The Astrophysical Journal, 980:102 (21pp), 2025 February 10 https://doi.org/10.3847/1538-4357/ada600

Investigating the Efficacy of Topologically Derived Time Series for Flare Forecasting. I. Data Set Preparation

Thomas Williams[1], Christopher B. Prior[1], and David MacTaggart[2]
[1] Department of Mathematical Sciences, Durham University, Durham, UK; tomwilliamsphd@gmail.com
[2] School of Mathematics & Statistics, University of Glasgow, Glasgow, UK
Received 2024 December 5; revised 2025 January 2; accepted 2025 January 2; published 2025 February 6

Abstract

The accurate forecasting of solar flares is considered a key goal within the solar physics and space weather communities. There is significant potential for flare prediction to be improved by incorporating topological fluxes of magnetogram data sets, without the need to invoke three-dimensional magnetic field extrapolations. Topological quantities such as magnetic helicity and magnetic winding have shown significant potential toward this aim, and provide spatiotemporal information about the complexity of active region magnetic fields. This study develops time series that are derived from the spatial fluxes of helicity and winding that show significant potential for solar flare prediction. It is demonstrated that time-series signals, which correlate with flare onset times, also exhibit clear spatial correlations with eruptive activity, establishing a potential causal relationship. A significant database of helicity and winding fluxes and associated time series across 144 active regions is generated using Space-Weather HMI Active Region Patches data processed with the Active Region Topology (or ARTop) code that forms the basis of the time-series and spatial investigations conducted here. We find that a number of time series in this data set often exhibit extremal signals that occur 1–8 hr before a flare. This publicly available living data set will allow users to incorporate these data into their own flare prediction algorithms.

Unified Astronomy Thesaurus concepts: Solar flares (1496); Solar active region magnetic fields (1975); Space weather (2037)

1. Introduction

The forecasting of solar eruptions is one of the most important practical issues in solar physics. Energetic particles from solar flares can damage/degrade the electronic components aboard satellites, while coronal mass ejections (CMEs) have crucial impacts on critical infrastructure such as radio communication, GPS signaling, and power grids. A recent international collaboration performed a systematic comparison of existing flare forecast methods (as well as developing the statistical and methodological tools for this comparison) (K. Leka et al. 2019a, 2019b). These methods are based on analyzing photospheric magnetograms, which provide information on the structure of the Sun's magnetic field as it passes from the interior into the solar atmosphere. The efficacy of the results is briefly summarized by the following text from K. Leka et al. (2019a):

"*Regarding the results, generally speaking, no method works extraordinarily well; but we demonstrate that a fair number of methods consistently perform better than various no-skill measures, meaning that they do show definitive skill across more than one metric*."

Similarly, M. K. Georgoulis et al. (2021) stated:

"*In spite of being one of the most intensive and systematic flare forecasting efforts to-date, FLARECAST has not managed to convincingly lift the barrier of stochasticity in solar flare occurrence and forecasting: solar flare prediction thus remains inherently probabilistic*."

In short, what these two studies reveal is that while significant progress has been made, there is still room for improvement.

Magnetic topology, which can be quantified by the magnetic helicity as a measure of the flux-weighted entanglement of a magnetic field, has long been used as a diagnostic tool in the analysis of solar active regions, e.g., E. Pariat et al. (2005, 2006, 2017), A. Nindos et al. (2003), Y. Liu & P. Schuck (2012), K. J. Knizhnik et al. (2015), E. R. Priest et al. (2016), F. P. Zuccarello et al. (2018), P. Vemareddy (2019), L. Liu et al. (2019), R. Wang et al. (2018), R. Jarolim et al. (2023), and K. Moraitis et al. (2024). The near perfect conservation of magnetic helicity in the corona means one can estimate the helicity content of active region fields from observational data (magnetogram data) via helicity fluxes at the photosphere (E. Pariat et al. 2005; S.-H. Park et al. 2010, 2021; P. Vemareddy 2019; M. Korsós et al. 2020; K. Alielden et al. 2023).

Recently, two of the authors of this study demonstrated the efficacy of a related quantity, the magnetic winding: the entanglement of the field measured without flux weighting, which can also be estimated from observational magnetogram data (C. Prior & D. MacTaggart 2020). It was shown to provide the first direct and unambiguous evidence of preexisting twisted field structure emerging into the solar corona (D. MacTaggart et al. 2021). It was also shown that imbalances in current-carrying magnetic entanglement of developing active region fields presaged the onset of flaring in a set of active regions (B. Raphaldini et al. 2022, 2023) and, in addition, that significant localized variance in these signatures often trailed large X-class flares by ≈ 7 hr, providing evidence of the potential for individual flare prediction. Finally in O. Aslam et al. (2024), it was shown that spikes in the input of magnetic winding correlated consistently both temporally and spatially with the onset of CMEs in 28 of 30 active regions.

To promote the routine use of both magnetic helicity and winding flux estimation, Active Region Topology (ARTop; K. Alielden et al. 2023) was released, an open-source software that can calculate both helicity and winding fluxes as well as various combinations and decompositions of these quantities. The package provides time series of the net values of these fluxes and also spatiotemporal time series of their density distributions in the regions. The aim of this study is to establish, based on a much expanded data set, the potential predictive efficacy of combinations of information produced by both the magnetic winding and helicity fluxes via ARTop with a particular focus on the spatial aspect of these distributions. In short, the ARTop package was aimed at generating meaningful spatiotemporal time series from this data, and this study aims to provide guidance as to how it might be used for flare prediction.

In Section 2, we present the methods adopted and data set analyzed in this study. In Section 4, a number of potential predictive quantities are investigated using three example active regions, while a more comprehensive data set is explored in Section 5. Finally, our conclusions are presented in Section 6.

2. Methodology

Following a similar procedure to that outlined in O. Aslam et al. (2024), we utilize two open-source codes, which are detailed below, to investigate how solar eruptions may be predicted. The first code calculates magnetic helicity and magnetic winding input rates at the photosphere and is written in C++ and python while the second code is an autonomous low-coronal CME detection code written in IDL. In the following subsections, the details of these two codes are summarized, while the full details on their respective methods can be found in K. Alielden et al. (2023) and T. Williams & H. Morgan (2022).

2.1. Active Region Topology

ARTop (K. Alielden et al. 2023) is an open-source tool for studying the input of topological quantities into solar active regions at the photospheric level. ARTop utilizes vector magnetograms (J. T. Hoeksema et al. 2014) from the Helioseismic and Magnetic Imager (HMI; J. Schou et al. 2012) aboard the Solar Dynamics Observatory in the form of Space-Weather HMI Active Region Patches (SHARP) to create maps, time series, and other metrics derived from input rates of magnetic helicity and magnetic winding fluxes (see C. Prior & D. MacTaggart 2020 for a detailed summary of their meaning and importance in solar applications). The flux of magnetic helicity has long been considered an important quantity in the study of active regions and solar flares (A. A. Pevtsov et al. 2003; S.-H. Park et al. 2008; P. Vemareddy 2021; M. Korsós et al. 2022; Y. Liu et al. 2023), the winding is a relativity novel quantity, which has been shown to have additional predictive efficacy (C. Prior & D. MacTaggart 2020; D. MacTaggart et al. 2021; B. Raphaldini et al. 2022; O. Aslam et al. 2024).

This study does not use all of the quantities calculated by ARTop and so the following only provides a brief overview of the critical quantities that are directly used here. The fundamental geometrical quantity considered is the rotational motion of field line footpoints at the photospheric surface P. Let $\boldsymbol{x}(t) = (x_1, x_2)$ and $\boldsymbol{y}(t) = (y_1, y_2)$ represent the position vectors in P of two field lines intersecting P at a time t. The mutual angle $\Theta(\boldsymbol{x}, \boldsymbol{y})$ of the two field line intersection points in P is given by

$$\Theta(\boldsymbol{x}, \boldsymbol{y}) = \arctan\left(\frac{y_2 - x_2}{y_1 - x_1}\right). \tag{1}$$

Its rate of rotation can be written as the in-plane motion of the footpoints $\boldsymbol{u}(\boldsymbol{y}) = (dy_1/dt, dy_2/dt)$, which is estimated using the DAVE4VM method (P. W. Schuck 2008), and a vector $\boldsymbol{r} = \boldsymbol{y} - \boldsymbol{x}$, joining the two points as

$$\frac{d\Theta(\boldsymbol{x}, \boldsymbol{y})}{dt} = \boldsymbol{e}_z \cdot \frac{(\boldsymbol{u}(\boldsymbol{x}) - \boldsymbol{u}(\boldsymbol{y})) \times \boldsymbol{r}}{|\boldsymbol{r}|^2}. \tag{2}$$

The magnetic winding input rate $d\mathcal{L}/dt$, associated with a point $\boldsymbol{x}$ in the photospheric plane P, is the average winding of that point with all other field line motions $\boldsymbol{y}(t) \in P$:

$$\frac{d\mathcal{L}}{dt}(\boldsymbol{x}) = -\frac{1}{2\pi}\int_P \frac{d\Theta(\boldsymbol{x}, \boldsymbol{y})}{dt}\, d^2y, \tag{3}$$

and the field line helicity input rate $d\mathcal{H}/dt$ is the winding weighted by the magnetic flux:

$$\frac{d\mathcal{H}}{dt}(\boldsymbol{x}) = -B_z(\boldsymbol{x})\frac{1}{2\pi}\int_P B_z(\boldsymbol{y})\frac{d\Theta(\boldsymbol{x}, \boldsymbol{y})}{dt}\, d^2y. \tag{4}$$

The minus signs represent the fact that P is the lower boundary of the domain in which the active region field exists (so the normal to P is opposite to the normal of that domain). As discussed in detail in C. Prior & D. MacTaggart (2020), this helicity input rate is the same as the relative helicity rates calculated in studies of photospheric helicity fluxes (S.-H. Park et al. 2008; P. Vemareddy 2021; M. Korsós et al. 2022; Y. Liu et al. 2023), and we simply emphasize its geometric underpinning. ARTop also provides the spatially integrated winding dL/dt and helicity dH/dt inputs as

$$\frac{dL}{dt} = \int_P \frac{d\mathcal{L}}{dt}(\boldsymbol{x})\, d^2x\,, \quad \text{and} \quad \frac{dH}{dt} = \int_P \frac{d\mathcal{H}}{dt}(\boldsymbol{x})\, d^2x, \tag{5}$$

from which the time-integrated inputs can be calculated as

$$L(t) = \int_0^t \frac{dL}{dt}dt, \quad \text{and} \quad H(t) = \int_0^t \frac{dH}{dt}dt. \tag{6}$$

Approximate helicity conservation implies that $H(t)$ should be a good estimate of the amount of helicity in the active region field above the photosphere (M. A. Berger 1984), and this manuscript focuses on how crucial this estimation can be for flare prediction, a fact which has previously been observed in other studies (B. LaBonte et al. 2007; S.-H. Park et al. 2008; R. Jarolim et al. 2023; S. H. Garland et al. 2024). It was shown in C. Prior & D. MacTaggart (2020), D. MacTaggart et al. (2021), B. Raphaldini et al. (2022), and O. Aslam et al. (2024) that the winding provides distinct and complementary information to the helicity, as the flux weighting in the helicity means it is dominated by magnetic field with a strong vertical component and twisted nature (i.e., the main poles) while the winding is largely dominated by the strong (dominantly) transversal field near the polarity inversion line (i.e., the top of sheared arcades or bald patch field).

Field line velocities can be estimated from magnetogram data by assuming ideal motion (E. Pariat et al. 2005). Under this assumption, the motion $\boldsymbol{u}(\boldsymbol{x})$ of the point of intersection of

Table 1
SHARP Regions Investigated with Flare Information Provided by the Heliophysics Event Knowledgebase

NOAA Active Region	SHARP Number	Largest Flare	No. X-class Flares	No. M-class Flares	No. C-class Flares	First Observation Time (UTC)
11158	377	X2.2	1	3	24	2011/02/10 22:58:11
11302	892	X1.9	2	15	30	2011/09/21 12:34:20
12673	7115	X9.3	3	12	20	2017/08/28 08:58:43

a field line and the photosphere can be written in terms of the field $\boldsymbol{B}$ and the plasma velocity $\boldsymbol{v}(\boldsymbol{x})$ (decomposed into out-of-plane v_z and in-plane $\boldsymbol{v}_\parallel$ components) as

$$\boldsymbol{u}(\boldsymbol{x}) = \boldsymbol{v}_\parallel(\boldsymbol{x}) - \frac{v_z(\boldsymbol{x})}{B_z(\boldsymbol{x})}\boldsymbol{B}_\parallel(\boldsymbol{x}) = \boldsymbol{u}_b + \boldsymbol{u}_e, \tag{7}$$

where $\boldsymbol{u}_b$ represents the plasma moving the field line ideally in-plane (braiding if adding to the winding), and the second term $\boldsymbol{u}_e$ represents the emergence/submergence of field. The velocity has implicit $\boldsymbol{B}$ dependence as it is determined by DAVE4VM using the magnetic field data. We highlight that this inversion has a crucial parameter associated with it. The magnetic field must be smoothed for the least-square matrix used in the inversion of the DAVE4VM method to be well defined; we term it velocity smoothing (VS) in ARTop. VS is the width (number of pixels) of the window surrounding the point of interest used to locally average the field. The velocity and helicity values can be significantly affected by this choice (P. W. Schuck 2008; Y. Bi et al. 2018; K. Alielden et al. 2023). The work presented here develops quantities whose predictive efficacy are as independent of this choice as possible.

The final critical quantities to introduce are those on which our metrics are based. It is possible to decompose the field into a potential part and a "current-carrying" part, i.e., the Helmholtz decomposition:

$$\boldsymbol{B}(t) = \boldsymbol{B}_p(t) + \boldsymbol{B}_c(t). \tag{8}$$

The potential part is uniquely determined by the B_z distribution on the photospheric boundary (B. Raphaldini et al. 2022; K. Alielden et al. 2023; see a discussion on the method used), which then gives $\boldsymbol{B}_c(t)$ from the observed in-plane components. Using these two fields, one can calculate current-carrying helicity and winding fluxes, $d\mathcal{H}_c/dt$ and $d\mathcal{L}_c/dt$, and potential fluxes, $d\mathcal{H}_p/dt$ and $d\mathcal{L}_p/dt$. Then, since we expect flaring to occur when there is a (local) imbalance toward current-carrying topology, ARTop calculates the following δ quantities:

$$\delta L(T) = \int_0^T \int_P \left(\left| \frac{d\mathcal{L}_c}{dt} \right| - \left| \frac{d\mathcal{L}_p}{dt} \right| \right) d^2y \, dt, \tag{9}$$

and

$$\delta H(T) = \int_0^T \int_P \left(\left| \frac{d\mathcal{H}_c}{dt} \right| - \left| \frac{d\mathcal{H}_p}{dt} \right| \right) d^2y \, dt, \tag{10}$$

which is positive if there is an imbalance toward current-carrying winding/helicity flux. In B. Raphaldini et al. (2022) and K. Alielden et al. (2023) it was shown the δ fluxes were only affected a small amount by the choice of VS; by contrast, it had quite a significant effect on the rates $d\mathcal{L}_c/dt$, $d\mathcal{H}_c/dt$, $d\mathcal{L}_p/dt$, and $d\mathcal{H}_p/dt$. This study provides further evidence that quantities based on the δ quantities are far more consistent with regards to flare prediction signals than the rates $d\mathcal{H}/dt$ and $d\mathcal{L}/dt$ themselves. In what follows, for the sake of notational brevity, we denote all rates with a dash, i.e., $\mathcal{H}' = d\mathcal{H}/dt$ or $\delta L' = d\delta L/dt$.

2.2. ALMANAC

As with O. Aslam et al. (2024), we also employ the Automated Detection of CoronaL MAss Ejecta origiNs for Space Weather AppliCations (ALMANAC) code (T. Williams & H. Morgan 2022) when focusing on specific events in time-series data to identify potential CMEs. ALMANAC, unlike many widely adopted CME detection methods, does not rely upon coronagraph data, but instead utilizes data from the Atmospheric Imaging Assembly (J. R. Lemen et al. 2012). The main advantage of ALMANAC is that it does not require geometrical fitting to approximate the CME source location in the low solar corona. Subsequently, the code does not inherently have large uncertainties due to projection effects caused by fitting a simple "wire-frame" of a three-dimensional object mapped in two dimensions. As such, ALMANAC provides a reliable low-coronal CME origin that is obtained independently of any helicity/winding signatures from the earlier phases of an eruption.

To detect potential Earth-directed CMEs, ALMANAC first crops the map size to eliminate off-limb contributions and standardizes the intensity across an 8 hr image sequence by thresholding intensities and normalizing the data values. It is then smoothed through convolution and subtracted from the normalized data to create a high-bandpass and time-filtered image sequence. Each time step of the time-filtered data is then divided by the median of the absolute values of the unfiltered data to eliminate contribution from "static" structures such as active regions. The method employs a series of Boolean masks to isolate connected clusters of pixels associated with a potential eruption, and spatiotemporal smoothing of these masks helps avoid the segmentation of regions. The first time step in which a region of sufficient size and duration is identified is used as the CME onset time, while the center of mass for the masked pixels at that time provides the central location for the CME. Full details of the method can be found in T. Williams & H. Morgan (2022).

3. Data Set

In Section 4, we initially analyze a subset of three active regions (Table 1). These examples are used to highlight some critical aspects underlying the construction of the new metrics presented in this work, before investigating some of the conclusions from this set on a much larger sample of 144 SHARP regions (see the Appendix for details). The 144 SHARP regions are curated from the data set outlined in A. Hollanda et al. (2021), where we ensured a number of X-class flaring regions are included. For the other regions included in this study, they have been sampled at somewhat regular time intervals to ensure an even coverage across the solar cycle. As the data set developed for this manuscript is a living data set, it will continually evolve as more of the regions outlined by A. Hollanda et al. (2021) are processed with ARTop. Of the 144 SHARP regions analyzed, 65 regions are considered to be flaring with a further 79 nonflaring regions. In this work, a region is considered to be flaring if an X-ray class flare of C1.0 or above is recorded in the Heliophysics Event Knowledgebase (HEK; N. E. Hurlburt 2022). Subsequently, the data set presented in this manuscript contains 1228 flares, which will continue to grow as more active regions are added to the living data set. An active region is sampled with a cadence of 720 s for the entire duration it is visible within the HMI data. This does mean that some regions will include periods where the position(s) exceed longitudes of $\pm 60°$ with respect to the central meridian. However, for the examples we focus upon in more detail, all of the analyses are conducted when the regions are within these longitudinal bounds. From these examples that we focus upon in greater detail in Section 4, two are what may be considered "classic" examples, such as AR 11158 and AR 12673, for their predictable behavior and propensity for large eruptions. The three regions we highlight to demonstrate new quantities that could potentially aid flare prediction are all distinctly different.

AR 11158 begins as a pair of aligned bipoles. As it evolves, the inner poles of each bipole are seen to interact and rotate, forming a more complex morphology. The topological properties of this region have been discussed in numerous studies (K. Tziotziou et al. 2013; E. Lumme et al. 2019; J. K. Thalmann et al. 2019; M. Korsós et al. 2022; R. Jarolim et al. 2023), while B. Raphaldini et al. (2022) provided a detailed comparison of the ARTop time-series analysis of this region in relation to those studies. These precise dynamics are not directly relevant to the results presented here, suffice to say all studies note significant helicity injection due to the mutual rotation of the inner poles and their subsequent interaction.

For the first 120 hr of AR 12673 observations, it is a single positive polarity pole, which undergoes a sudden emergence of positive and negative magnetic field, with the negative field wrapping around the active region, forming multiple strong polarity inversion lines that expand rapidly as a new emergent field "pushes" the existing field into opposite polarity structures. As with AR 11158, the topological properties of this region have been discussed in numerous studies (K. Moraitis et al. 2019; D. J. Price et al. 2019; J. K. Thalmann et al. 2019; P. Vemareddy 2019; K. Kusano et al. 2020; M. Korsós et al. 2022), and a detailed comparison of the ARTop time-series analysis of this region by comparison to those studies is conducted in B. Raphaldini et al. (2022). The analysis of a large spike in the winding flux time series just prior to the two-large X-class flares that were shown to spatially coincide with a flux rope in a nonlinear force-free field extrapolation of this region performed by K. Kusano et al. (2020) is of particular interest. It was shown that the spike coincided with a downflow (negative velocity plasma flow) in a region with a highly concentrated shear.

As for AR 11302, this is largely bipolar with some parasitic negative polarity field in the center of the region that encompasses a portion of the positive polarity field. As the region evolves, the positive polarity disperses into a diffuse field, with the negative polarity pole bifurcating into several smaller "poles" before it is swept beyond HMI's field of view.

These three regions provide a varied basis upon the conditions for flaring to occur, and thus serve as the initial testing for the feasibility of quantities to be flare predictors. The three active regions (Table 1) are then analyzed to quantify the flaring in relation to the parameters discussed throughout Section 4. In Section 5, we further explore these parameters on a more complete data set that is detailed in the Appendix.

4. Determination of Meaningful Quantities

4.1. Velocity Smoothing and Downsampling

In this subsection, the focus is on differences detected when utilizing different parameter values within the ARTop code. To highlight these differences, we focus on the large eruption associated with NOAA AR 11158, which led to an X2.2 solar flare and sympathetic CME 4 minutes later that was detected in SOHO/LASCO data (O. Aslam et al. 2024), as indicated in Figure 1 on various ARTop derived time series. In addition to this large eruption, ALMANAC also detected two smaller CMEs that occurred 1.25 hr prior to, and 1.67 hr post the X2.2 eruption, respectively. This is one example, from a set of 30 events in O. Aslam et al. (2024), of a CME event that was shown to be presaged by a significant spike in the rate $\mathcal{L}'$. These spikes were also correlated to key magnetic structures in extrapolations of the field; hence, they are shown to be physically meaningful.

As is discussed in Section 2.1, ARTop utilizes the DAVE4VM method to calculate velocity from noisy magnetogram data, which employs a VS. The value of VS represents a padding of typically between 11 and 20 pixels (P. W. Schuck 2008; D. MacTaggart et al. 2021) surrounding the pixel for which a velocity is being determined. In K. Alielden et al. (2023, their Figure 5), an example is shown for values of VS = 12 and 20 pixels that indicates no significant difference in the general behavior of the time series for the topological quantities calculated. In B. Raphaldini et al. (2022), it was found, however, that some quantities derived from these calculations can show significant differences depending on this choice. The finding from B. Raphaldini et al. (2022) is that the quantity $\delta\mathcal{L}'$ is relatively consistent with this value, a finding we elaborate on here. In Figure 1, we highlight differences in the time at which a peak is seen for VS = 12 (green) and 20 (orange) pixels in the magnetic winding rate over both of its decompositions into current-carrying and potential components. The most notable difference here is the example of $\mathcal{L}'$ (and $\mathcal{L}'_c$) utilizing VS = 20, which display significant peaks prior to the eruptions that are not captured until post-eruption for VS = 12 pixels (gray circles in Figure 1). As with K. Alielden et al. (2023), Figure 1 highlights that the downsampling factor, D applied to increase the processing speed of ARTop has negligible effects on these quantities (blue, $D = 1$; orange, $D = 3$).

In Figure 1, the input rates of $\delta\mathcal{L}'$, $\mathcal{L}'$, $\mathcal{L}'_c$, and $\mathcal{L}'_p$ for various choices of the parameters VS and D are presented. Crucially, this indicates that $\delta\mathcal{L}'$ is not particularly sensitive to the choice of VS and D made during data processing with ARTop, as all three time-series exhibit temporally coincident peaks that are immediately before the X2.2 flare and CME (pink circle in Figure 1). Unlike the other magnetic winding parameters

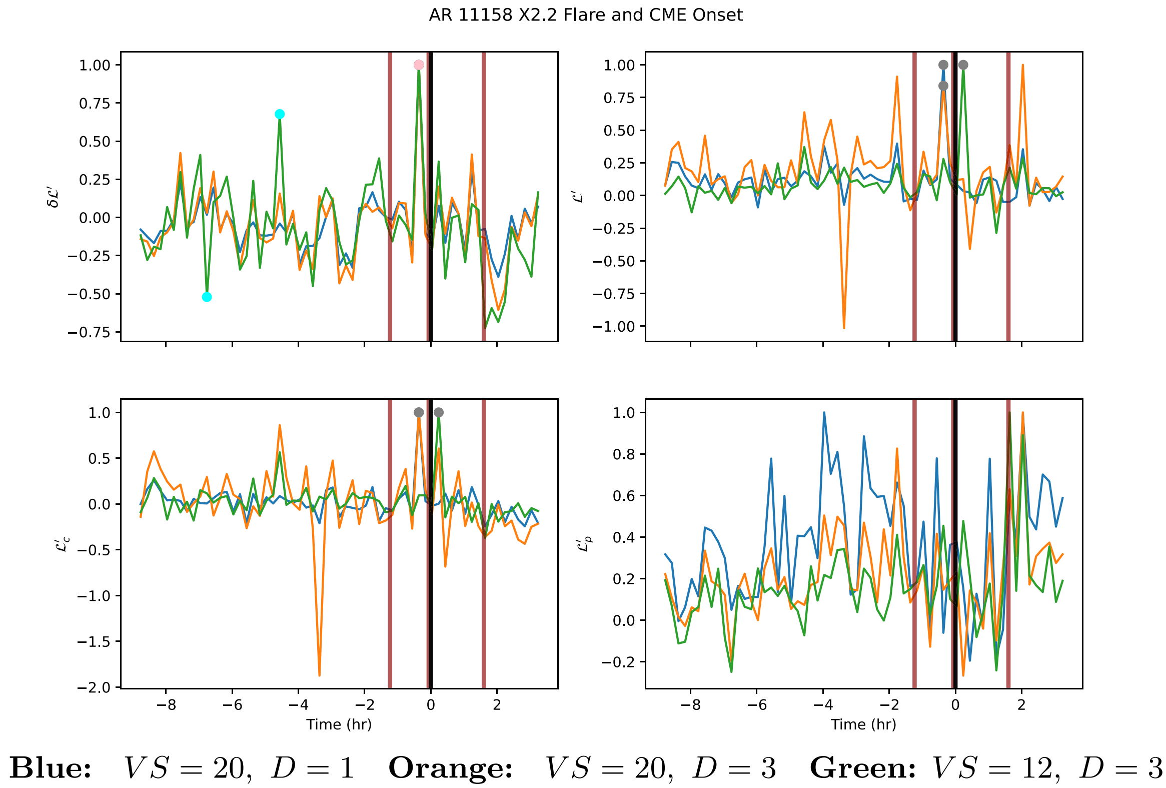

Figure 1. Shown here is the time-series evolution for topological quantities $\delta\mathcal{L}_c^{'}$, $\mathcal{L}'$, $\mathcal{L}_c^{'}$, and $\mathcal{L}_p^{'}$ before and after the X2.2 flare and sympathetic CME of AR 11158 for various velocity smoothing (VS) and downsampling (D) values. All plots are normalized with respect to their largest value. The X2.2 flare start time has been taken as Time = 0, which is indicated in black with the CME onset times reported by ALMANAC shown in red. The gray, pink, and cyan circles denote the peaks discussed in the manuscript where spikes are (or not) shifted due to the choice of VS. Blue series correspond to VS = 20, $D = 1$; orange series correspond to VS = 20, $D = 3$; while green series represent VS = 12, $D = 3$ for the $\delta\mathcal{L}'$ (top left), $\mathcal{L}'$ (top right), $\mathcal{L}_c^{'}$ (bottom left), and $\mathcal{L}_p^{'}$ (bottom right) time series.

shown, all time series typically peak and trough at the same time often with similar magnitudes. There are, however, instances such as Time ≈ -6.5 hr and ≈ -4.5 hr where the peak (trough) in the data processed with VS = 12 (cyan circles in Figure 1) is larger than the peaks (troughs) seen for the two VS = 20 calculations.

Since the choice of the parameter VS is somewhat arbitrary (and has taken numerous different values in the literature), we make the decision to base the metrics we develop in what follows on the parameter δL, which is the least sensitive to this choice. This decision was validated by verifying that the database of physically meaningful spikes in O. Aslam et al. (2024) also exhibits spikes in $\delta\mathcal{L}'$ at the same times found in this study.

4.1.1. Decomposing $\delta\mathcal{L}'$ and $\delta\mathcal{H}'$

The main implication of the result shown in Figure 1 is that the decomposition of magnetic winding (and magnetic helicity) into components for current-carrying and potential topology is sensitive to the parameter VS. Given the lack of sensitivity of $\delta\mathcal{L}'$ to these parameters, we instead split $\delta\mathcal{L}'$ and $\delta\mathcal{H}'$ into positive and negative components whereby positive (negative) would indicate that the dominant input of topology at the photospheric level is current-carrying (potential) topology. This is achieved by turning Equations (9) and (10) into conditional expressions, such that

$$\delta\mathcal{L}_c^{'} = \begin{cases} \delta\mathcal{L}', & \text{if } \delta\mathcal{L}' > 0 \\ 0, & \text{otherwise,} \end{cases}$$
$$\delta\mathcal{H}_c^{'} = \begin{cases} \delta\mathcal{H}', & \text{if } \delta\mathcal{H}' > 0 \\ 0, & \text{otherwise,} \end{cases} \tag{11}$$

and

$$\delta\mathcal{L}_p^{'} = \begin{cases} \delta\mathcal{L}', & \text{if } \delta\mathcal{L}' < 0 \\ 0, & \text{otherwise,} \end{cases}$$
$$\delta\mathcal{H}_p^{'} = \begin{cases} \delta\mathcal{H}', & \text{if } \delta\mathcal{H}' < 0 \\ 0, & \text{otherwise.} \end{cases} \tag{12}$$

Thus, these decompositions can be used to focus solely on the net input of either current-carrying-dominant topology ($\delta\mathcal{L}_c'$, $\delta\mathcal{H}_c'$) or potential-field-dominant topology ($\delta\mathcal{L}_p'$, $\delta\mathcal{H}_p'$) at the photosphere (rather than allowing the two to cancel as in the series $\delta\mathcal{L}$). It has previously been demonstrated that it is the current-carrying component of $\mathcal{L}'$ that is likely responsible for disrupting an existing magnetic field in the solar atmosphere that leads to an eruption (as in E. Pariat et al. 2017; B. Raphaldini et al. 2022) and so we will consider time series of based upon $\delta\mathcal{L}_c'$ and $\delta\mathcal{H}_c'$ here.

In Figure 2, $\delta\mathcal{L}_c'$ time-series plots are shown for three example SHARP regions over 72 hr periods that include a range of C- to X-class flares, which are used to highlight some

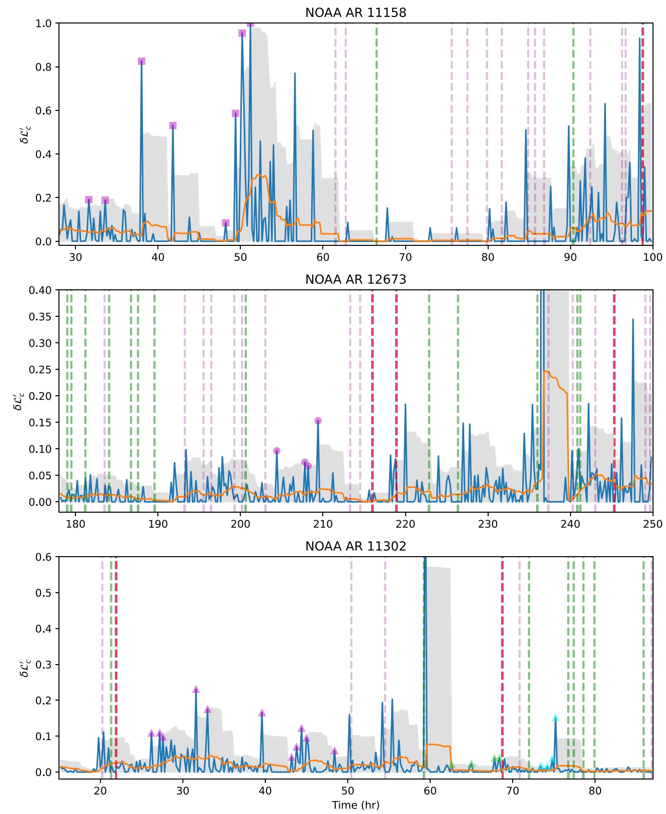

Figure 2. Time-series plots for $\delta\mathcal{L}_c'$ (blue) with a running mean of 3 hr (orange) and 2σ envelope (gray) for three SHARP regions preceding M- (dashed green) and X-class (dashed red) solar flares. For context, C-class flares are also shown (dashed pink). Each plot is normalized with respect to the maximum spike in the time series.

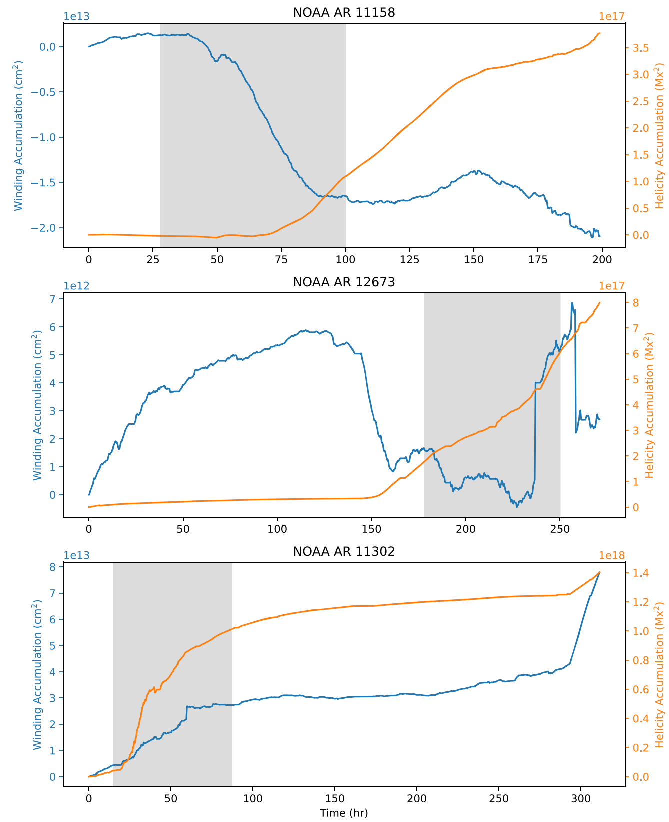

Figure 3. The time-integrated quantities $\delta\mathcal{L}'$ (blue) and $\delta\mathcal{H}'$ (orange) calculated for active regions NOAAs 11158, 11302, and 12673. The shaded gray regions indicate the 72 hr observation windows shown in Figure 2 for each active region. The large increases seen in the winding accumulation, and to a lesser extent helicity accumulation, toward the end of the observed time for AR 11302 and AR 12673 are caused by projection effects in the SHARP data due to the active regions exceeding longitudes of 60°.

of the properties of this quantity with regards to the potential for flare prediction. A 3 hr running mean and corresponding 2σ envelope are calculated for each series, which are used to determine significant spikes/peaks in the time series that could lead to an eruption (B. Raphaldini et al. 2022; O. Aslam et al. 2024). Here, a spike, or an extremal event, is defined as a point in time when the time series in question exhibits a value outside the 2σ envelope.[3]

Focusing first on NOAA AR 11158, we see there are eight spikes during Time $= 30-55$ hr (magenta squares) that are not followed by flaring within $6-12$ hr of a spike, while the majority of spikes indicated beyond this time either precede large M- and X-class flares or they are followed by multiple smaller C-class eruptions within $6-12$ hr. This suggests one needs additional information to determine if such spikes in a time series are (potentially) meaningful. To this end, analysis of the time-integrated quantities $\delta\mathcal{L}$ and $\delta\mathcal{H}$ (Figure 3) reveals that the spikes are only followed by flares (within a $6-12$ hr period) after there has been a significant cumulative input of current-carrying helicity. One possible interpretation of this observation is that the spikes in $\delta\mathcal{L}_c'$ seen between Time $=$ 30–55 hr (Figure 2) are not meaningful, as there is insufficient complex overlaying magnetic field structure to disrupt and initiate flaring. We investigate this particular period in more detail later when assessing spatial correlations between events.

This observation is supported by the activity in the case of AR 12673; we highlight a period between 180 and 250 hr where we see in Figure 3 that there has already been significant net current-carrying helicity input δH. In this case, almost all spikes can be correlated with a flare given a window of approximately 6 hr. We now focus on one specific set of signals within this window. First between $\approx$203 hr and $\approx$210 hr, where there are relatively large spikes (magenta circles) in the time series that exceed their 2σ envelope (but no flares until $\approx$213 hr to $\approx$220 hr), whence there are two C-class and two X-class flares; the largest apparent gap in this series between a set of spikes and a flare. This contrasts significantly to the period before, 180–200 hr, where there is a relatively steady occurrence of both smaller spikes and flares. These highlight the possibility of a pause in activity during which significant buildup of topology leads to the two significant X-class flares. We investigate this period in more detail later in the study when we focus on spatiotemporal correlations.

For AR 11302 (bottom panel of Figure 2), the first X-class flare emitted occurs during the "buildup" phase of the active region (around 21 hr), which is denoted by the fact that the cumulative winding (Figure 3) continually increases until time $\approx$70 hr, after which point the gradient flattens and a "steady-state" is reached (such as is discussed in B. Raphaldini et al. 2022). Initially, this event appears somewhat unusual, as our rough assumption from the previous examples is that active regions require time to develop complex topology before larger

[3] It is worth noting that the selection of the envelope is somewhat arbitrary, with B. Raphaldini et al. (2022) utilizing 3σ, while O. Aslam et al. (2024) demonstrates that 2σ is a reliable threshold for a sample of 30 different active regions.

eruptions occur. However, ARTop does not observe AR 11302 from its initial emergence as the active region rotates into view already partly developed, meaning the time-integrated inputs are not truly reflective of the total amount of helicity/winding injected into the region. This provides an example for one of the potential issues with building a predictive flaring model from photospheric topology inputs alone. That is, if an active region comes into view by rotation whereby a significant portion of the active region emergence phase has already occurred, then some additional function or method must be used to approximate the complex topology that has already been inputted into the solar atmosphere. One such possible method would be to use nonlinear force-free field extrapolations to estimate the topology in the region as early as possible as in R. Jarolim et al. (2023). From the standpoint of eventually developing a live predictive flare model, the fact there is a lull in flaring (Time $\approx 20-50$ hr) is also of interest. It seems the first X-class flare may have resulted in a significant decrease of complex topology above the photosphere, and so one might infer that additional complexity must be rebuilt again prior to additional eruptions occurring. Thus, when building a live predictive flare model based on helicity/winding calculations, one would need to account for the decrease in complex magnetic field within the active region after an eruptive event, as this is something that cannot be accounted for from photospheric calculations alone. However, it might be possible to estimate/account for the loss of complex field from the size of the flare alone with the adoption of additional quantities explored later in this manuscript and machine learning.

Later in the AR 11302 time series, when significant current-carrying helicity has been injected into the region, we see another interesting feature of these time series: There are some relatively small-amplitude spikes (green triangles) that precede relatively strong M- and X-class flares. By contrast, we later see three "small" and one "large" spike (cyan triangles) that are seen to precede a burst of four M-class flares in an $\approx$4 hr period. There does not seem to be a clear correlation between the magnitude of a spike and the magnitude of the flare following it. We do note, however, in the case of the X-class flare, that prior to this event at $\approx$69 hr there is a significant input of $\delta L'$ about 10 hr prior. This could potentially indicate that if information is included from a larger time window, there may have been some indication of the potential for a large flare. We shall explore this event in more detail later in the study.

4.1.2. Discussion

From these example calculations, we have seen a number of interesting properties that will be investigated further in the rest of the study.

1. There are very often extremal spikes in the rates of current-carrying-dominant topology input, $\delta\mathcal{L}_c'$ and $\delta\mathcal{H}_c'$, in a period up to 12 hr prior to flaring, with 69.7% of $\delta\mathcal{L}_c'$ spikes, and 65.3% of $\delta\mathcal{H}_c'$ spikes preceding flares in the three example regions.
2. These spikes correlate better to flaring activity when there has been a significant buildup of (non potential field) helicity in the region. For example, when helicity accumulation exceeds 1×10^{19} Mx^2, spikes preceding flares increase to 78.5% and 76.9% for $\delta\mathcal{L}_c'$ and $\delta\mathcal{H}_c'$, respectively.
3. If the initial emergence phase of the region is not captured in the data, it may be necessary to invoke additional information to estimate the helicity in the field when it emerges into view.
4. The magnitude of these spikes alone does not seem to correlate well with the size of the flare, which lies in its 6 hr post-spike window. Subsequently, more information is required to make specific predictions on flare magnitude.

4.2. The Input and Loss of Magnetic Topology

As this manuscript has detailed in Section 4.1.1, the excess current-carrying topology for magnetic helicity and magnetic winding was shown to be a promising candidate as a flare precursor. However, these metrics alone do not provide information on whether the fluxes associated with these quantities seen at the photospheric level are due to a new magnetic field emerging from within the solar interior, or whether it is because of a disturbance in the solar atmosphere that causes the existing field to be "pushed" to the photospheric level and/or below. The significance of knowing this information is that it may allow for more interpretation/understanding of the signals (significant spikes) produced by the ARTop time series. To this end, the current-carrying components of the delta measures for winding and the helicity can be combined with the line-of-sight velocity to form, $v_z\ \delta\mathcal{L}_c'$, and $v_z\ \delta\mathcal{H}_c'$ that quantify the speed and direction of magnetic topology input at the photosphere. While the quantities $\delta\mathcal{L}_c'$ and $\delta\mathcal{H}_c'$ are themselves fluxes (rates of input), they represent horizontal motion of field lines, so this quantity combines information about the vertical rise of the fluid transporting the field, with this information about the in-plane motion. Large spikes (dips) in these quantities indicate rapidly emerging (submerging) fluxes at the photospheric level.

In Figure 4 we show three time series of the quantity $v_z\ \delta\mathcal{L}_c'$ to highlight some of its properties. For AR 11158 (top panel), there are multiple emergence and submergence events that follow each other in quick succession during the buildup phase (i.e., time < 60 hr or with a larger time gap 37 and 42 hr). The submergence events are indicative of motions occurring within the solar atmosphere that push topology down to the photospheric level, indicating that some of the topology buildup seen in Figure 2 could be due magnetic structure already emerged through the photosphere. Similarly, in the $\delta\mathcal{L}_c'$ time series for AR 12673 (Figure 4), there are multiple pairs of opposing-sign spikes, some of which are coincident with the X-class flares or (temporally) contain M-class flares. Spatial maps for $v_z\ \delta\mathcal{L}_c'$ are shown (Figure 5) for an example submergence and reemergence of the first X-class flare in the AR 12673 time series (whose spatial location is indicated with a green plus). It is clear from these successive maps that material is pushed to the photospheric level or lower in a localized region around $(114°, -8°)$ by this flare, which then rebounds and pulls more photospheric material/field into the solar atmosphere, in the vicinity of the second X-class flare (location indicated by the green triangle). These events are discussed in more detail in Section 4.3.2. In a similar vein, the upflow/downflow events can be seen in AR 11302 at times $\approx$40 hr, $\approx$50 hr, and $\approx$70–75 hr in the bottom panel of Figure 4, with the latter event preceding M-class flares.

These phases of emergence and submergence causing winding topology to be seen at the photospheric level are

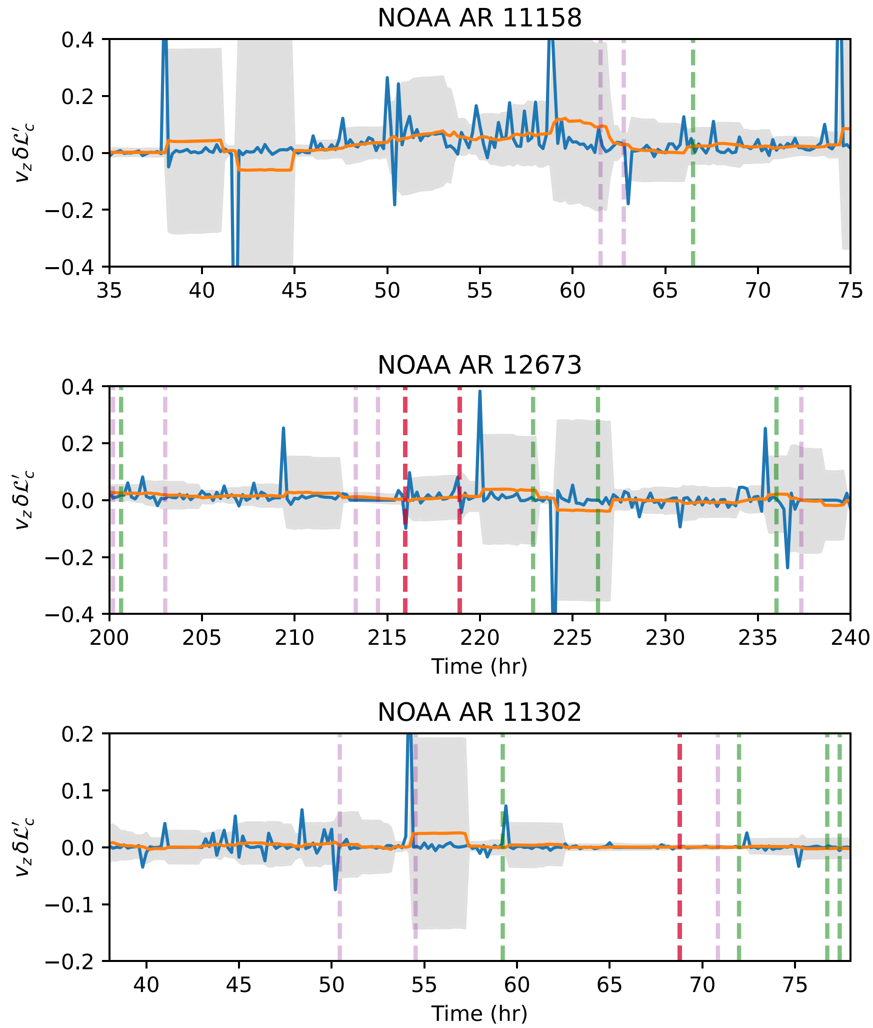

Figure 4. The time-series plots for the combined quantity, $v_z\ \delta\mathcal{L}'_c$ focusing upon the period leading up to the onset of flaring for AR 11158 and the X2.2 and X9.3 flares in AR 12673. The 3 hr running means (orange) and 2σ envelope (gray) are also shown along with the times of C- (dashed pink), M- (dashed green), and X-class (dashed red) flares.

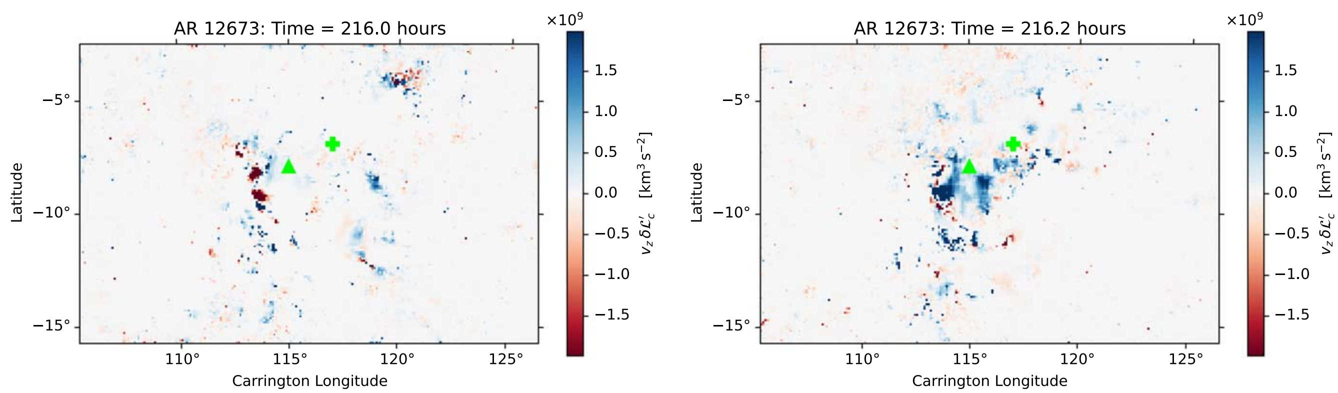

Figure 5. AR 12673 $v_z\ \delta\mathcal{L}'_c$ maps that correspond to the submergence and reemergence of topology seen for the first X-class flare (green plus) at time = 216 hr (first dashed red line in Figure 4). The position of the second X-class flare is also indicated (green triangle).

likely separate or interconnected structures where the emergence/submergence of one structure leads to buffeting of magnetic field, causing neighboring structures to emerge and submerge. As is highlighted in the AR 11158 $v_z\ \delta\mathcal{L}'_c$ time series, it appears that a period of emergent topology is required to induce flaring, and so focusing upon the net sign of emergence/submergence may provide additional insight to the likelihood of flaring within flare prediction models.

4.3. Spatial Significance of Temporal Spikes

The results from Figures 2 and 4 indicate that excess current-carrying topology quantities (e.g., $\delta\mathcal{L}'_c$) have the potential to be

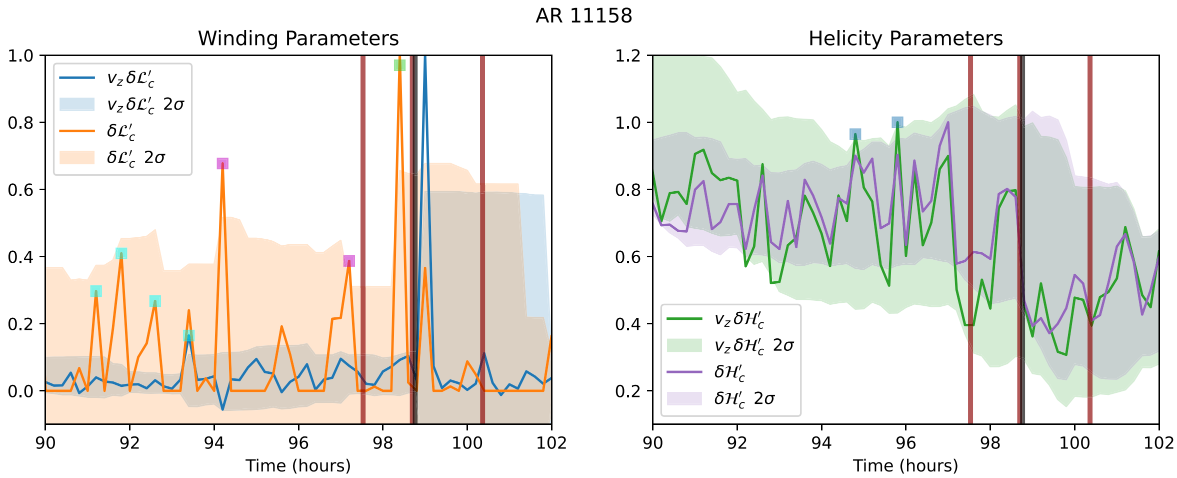

Figure 6. Left: time-series plots for $v_z\ \delta\mathcal{L}'_c$ (blue) and $\delta\mathcal{L}'_c$ (orange) from the same period as Figure 1 with the corresponding 2σ envelopes denoted by the shaded regions of the same colors. Right: time-series plots for $v_z\ \delta\mathcal{H}'_c$ (green) and $\delta\mathcal{H}'_c$ (magenta) from the same period as left with the corresponding 2σ envelopes denoted by the shaded regions of the same colors. The X2.2 flare is indicated by the black vertical line and the three CMEs detected by ALMANAC are shown in red.

precursive metrics for flaring, provided enough complex magnetic topology has been built up in the solar atmosphere. The variation in time frame for these precursors ranges between virtually immediate to potentially providing several hours of warning about the possibility of eruptive events taking place. This subsection analyses the spatial distribution of these two types of warnings, focusing on some of the X-class flares for the active regions given in Table 1.

4.3.1. AR 11158: Spatially Meaningful Spikes

In Figure 6, time series are presented for the current-carrying parameters for both winding and helicity prior to the X2.2 flare and a coincident CME that is detected in LASCO data. Furthermore, within the 12 hr period shown, ALMANAC detected two additional CMEs, the first of which is preceded by significant $\delta\mathcal{L}'_c$ spikes seen at time $\approx$ 94 and 97 hr (magenta squares). The first spike of the two indicated by magenta squares here is caused by a submergence event (negative $v_z\ \delta\mathcal{L}'_c$ at this time), indicating that a change in atmospheric topology caused the magnetic field to be pushed down to the photospheric level, highlighting how $v_z\ \delta\mathcal{L}'_c$ may be utilized to infer/capture information about the topological behavior above the photosphere. There is a spike (green square) at 98.4 hr that just precedes the coincident flare and CME. There is also an earlier spike in $v_z\ \delta\mathcal{L}'_c$ about 1 hr before the first $\delta\mathcal{L}'_c$ spike that indicates an emergence event. For the helicity parameters, $v_z\ \delta\mathcal{H}'_c$ exhibits two spikes between 94 and 96 hr (blue squares), while in the hour leading up to the first CME, $\delta\mathcal{H}'_c$ has a sharp decrease before the first, small CME takes place, with the input rate being somewhat constant before this. A similar trend is also seen with the X2.2 flare and associated CME, though the decline is coincident with the two eruptions in this example.

In Figure 7, the surface maps for one $v_z\ \delta\mathcal{L}'_c$ (a), three $\delta\mathcal{L}'_c$ (b), two $v_z\ \delta\mathcal{H}'_c$ spikes (c) highlighted in Figure 6 are shown. The CME at time $\approx$ 97.5 hr and the event composing an X2.2 flare and CME shortly afterward are denoted by the green triangle and green plus, respectively. The two first $\delta\mathcal{L}'_c$ spikes occur prior to the first small CME captured by ALMANAC (green triangle); the spatial maps of the fluxes $\delta\mathcal{L}'_c$ and $v_z\ \delta\mathcal{L}'_c$ for these times are shown in rows 1 and 2 of Figure 7(b). We see the primary input of topology occurs in the vicinity of (29°, -20°) just to the right and below the location of the first CME (triangle). The CME captured by ALMANAC propagates in a northerly direction across the solar disk, which, along with the center of mass for the first frame of detection, is why the authors believe these winding signatures contributed to the first eruption. In Figure 7(c), the $\delta\mathcal{H}'_c$ and $v_z\ \delta\mathcal{H}'_c$ input rates at the photosphere (temporally between the first two $\delta\mathcal{L}'_c$ maps of Figure 7(b)) indicate that topology is not only being built up at (29°, -21°), where the strong winding flux up was seen, but also either side of the location of the later X2.2 flare and CME, with a much stronger contribution in $v_z\ \delta\mathcal{H}'_c$ at (35°, -20°). Chronologically, the last maps (bottom panels of Figure 7(b)) reveal large-scale input of topology in the vicinity of the X2.2 flare and CME. The winding contribution for this event has been well documented in O. Aslam et al. (2024).

Solely analyzing $\delta\mathcal{L}'_c$ and $\delta\mathcal{H}'_c$ in this instance indicates some precursive warning on the potential for eruptions with up to $\approx$3 hr lead-time for the small CME and X2.2 flare events. However, the inclusion of $v_z\ \delta\mathcal{L}'_c$ provides further advanced warning. Prior to time = 94 hr, there are four spikes in $\delta\mathcal{L}'_c$—denoted by the cyan squares in Figure 6—that do not exceed their 2σ envelope due to previous signatures (although only just). The last of these spikes is associated with strong v_z values, and subsequently, $v_z\ \delta\mathcal{L}'_c$ is able to provide an additional 0.8 hr warning due to the low velocities associated with the other spikes resulting in a smaller 2σ envelope. We see in Figure 7(a) that these occur in the same location as the spikes in the first two rows of Figure 7(b) and can be attributed to the first CME event (green triangle). These events occur up to 7 hr before the CME, indicating some earlier warning could be detectable in the time series.

4.3.2. AR 12673: Destabilizing Events

In Figure 8, large coincident spikes in $\delta\mathcal{L}'_c$, and $v_z\ \delta\mathcal{L}'_c$ can be seen (magenta square), which precede a CME detected by ALMANAC by $\approx$4 hr. Second, coincident spikes are seen shortly before the X2.2 flare and CME (green square); additionally, a solitary spike in $\delta\mathcal{L}'_c$ (cyan square) that occurs before the slowly rising filament eruption that immediately precedes, and potentially triggers, the X9.3 flare is also seen. For the helicity, there is again some warning to the first CME, though much later and smaller in magnitude than the winding

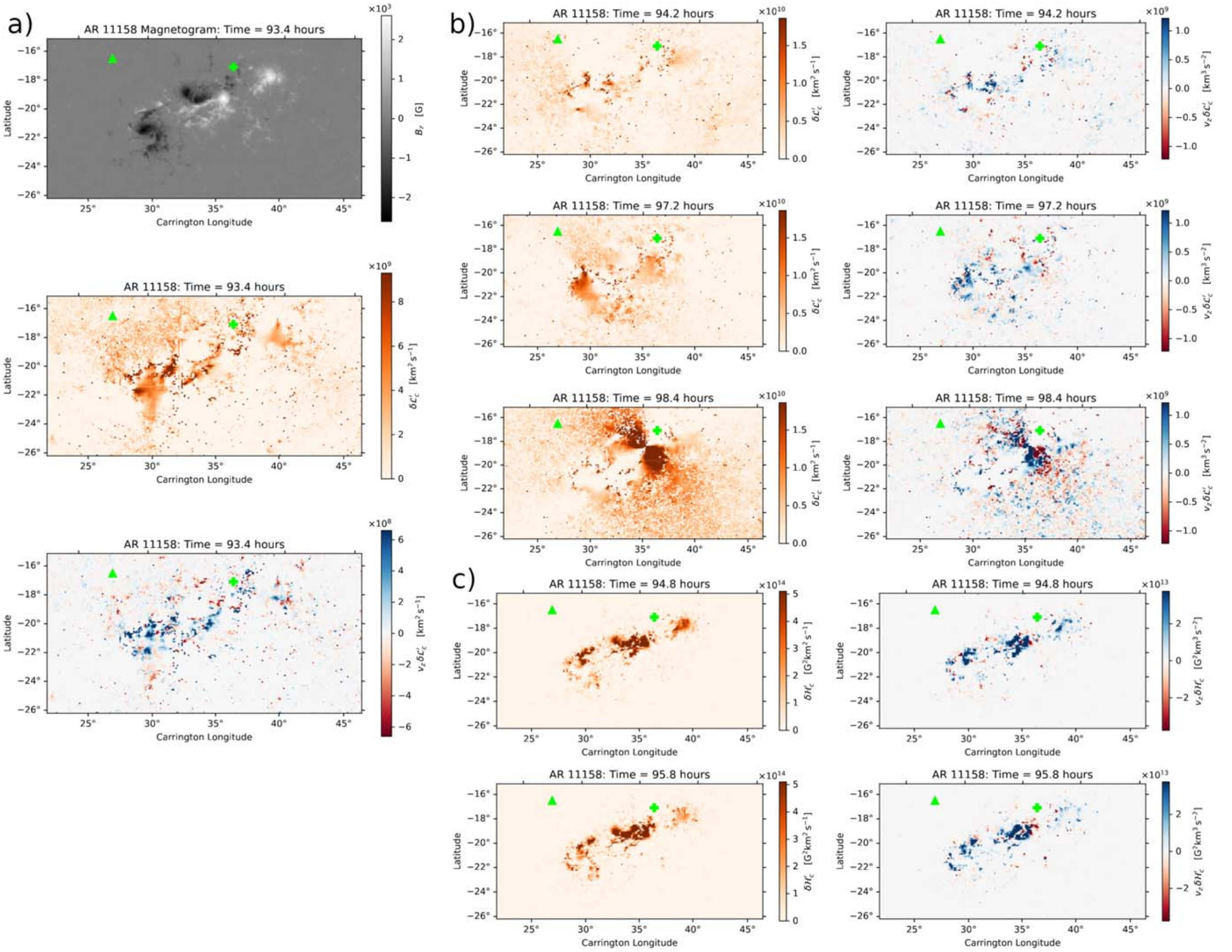

Figure 7. (a) HMI magnetogram and spatial maps for $\delta\mathcal{L}'_c$ and $v_z\ \delta\mathcal{L}'_c$ that corresponds to the fourth cyan square in Figure 6. (b) Spatial maps for $\delta\mathcal{H}'_c$ (left) and $v_z\ \delta\mathcal{H}'_c$ (right) corresponding to the spikes denoted by the blue squares in Figure 6. (c) The maps for $\delta\mathcal{L}'_c$ (left) and $v_z\ \delta\mathcal{L}'_c$ (right) corresponding to the spikes denoted by the magenta and green squares in Figure 6. The second (third) row corresponds to the surface maps immediately before the first (second) eruption. The positions of the first and second CMEs detected by ALMANAC are shown by the green triangle and the green plus in all panels, respectively.

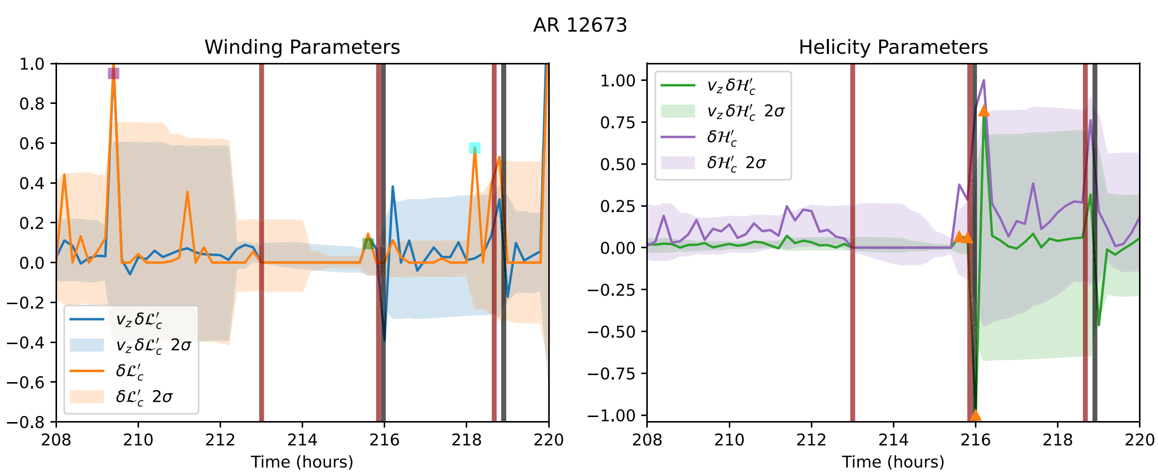

Figure 8. Left: time-series plots for $v_z\ \delta\mathcal{L}'_c$ (blue) and $\delta\mathcal{L}'_c$ (orange) for the hours leading to, and including, the X2.2 and X9.3 flares (times ≈ 216 and 219 hr) with the corresponding 2σ envelopes denoted by the shaded regions of the same colors. Right: time-series plots for $v_z\ \delta\mathcal{H}'_c$ (green) and $\delta\mathcal{H}'_c$ (magenta) from the same period as Figure 1 with the corresponding 2σ envelopes denoted by the shaded regions of the same colors. The X-class flares are indicated by the black vertical lines, and the three CMEs detected by ALMANAC are shown in red.

signature ($\approx$209.5 hr compared to $\approx$211 hr). Interestingly, $\delta\mathcal{H}_c'$ has a spike exceeding its 2σ envelope that is cotemporal with the winding signature spikes, which then further increases after the X2.2 flare and CME (orange triangles). For $v_z\ \delta\mathcal{H}_c'$ (and $v_z\ \delta\mathcal{L}_c'$), there is a prominent submergence during the eruption that is immediately followed by an emergence with both these events exceeding their envelopes in $v_z\ \delta\mathcal{H}_c'$ and $v_z\ \delta\mathcal{L}_c'$ (orange triangles).

Following the magnetic field model of D. J. Price et al. (2019) for AR 12673, there are two separate flux ropes that reside close to one another that (1) closely match the submerging/reemerging winding signatures, and (2) are the structures that are responsible for the X2.2 flare and CME. The first row of Figure 9 shows the winding maps for $\delta\mathcal{L}_c'$ and $v_z\ \delta\mathcal{L}_c'$, which reveal that the large spike denoted by the magenta square in Figure 8 is the result of a large region of strong topology primarily emerging at the photospheric level. Following the modeling of this region by D. J. Price et al. (2019), the strong emergence seen here between $(112° - 117°,\ -13° - 10°)$ is a low-lying null point that emerges between two preexisting, overarching flux ropes, further increasing the complexity of the magnetic field for the active region. Thus, when additional topology emerges beneath the flux ropes, as shown in the middle row just prior to the X2.2 flare and CME, and then in the bottom row just prior to the X9.3 flare, the events follow shortly after, as the emerging structures destabilize an already complex field.

4.3.3. AR 11302: Consequential and Inconsequential Spikes

For AR 11302, we focus upon the X1.9 flare ($\approx$69 hr). In the hours leading up to this event, the topological input has numerous significant potential contributions, as can be seen, for example, between time $\approx$ 62 hr and 69 hr in both the $\delta\mathcal{L}_c'$ and $\delta\mathcal{H}_c'$ plots (Figure 10). Additionally, unlike the other regions showcased in this manuscript, the X1.9 flare at $\approx$69 hr is preceded by relatively small spikes in both the winding and the helicity parameters, when compared to the rest of the time series (see Figure 2). We note these plots also exhibit relatively flat gradients during this period. The spatial distributions associated with these four spikes (magenta and green squares in Figure 10), are shown spatially in Figure 11(b). For the first two snapshots, shown in the first two rows of Figure 11(b), we see spatially that the concentrations of winding parameters are within the locality of the X1.9 flare, which is indicated by the lime green plus. By contrast, the latter two snapshots immediately before the eruption do not seem to have a spatial correlation with the event, as shown in the bottom two rows of Figure 11(b). Furthermore, it appears they are only seen as significant spikes due to the paucity of current-carrying topological input in the period prior. Subsequently, the warning about the X1.9 eruption is more physically meaningful from the spatiotemporal investigation of $v_z\ \delta\mathcal{L}_c'$ than $\delta\mathcal{L}_c'$ alone here.

Focusing upon the smaller spikes; in the first case (row 3), there are no strong spatial signatures in $\delta\mathcal{L}_c'$ or $v_z\ \delta\mathcal{L}_c'$. By contrast, in the second case (row 4), there is a signature seen at $(287°,\ 13°)$ (Figure 11(b), snapshot 4) that shows some spatial agreement with the strong helicity inputs show in Figure 11(c). These correspond to the spikes (blue squares in Figure 10) seen in $v_z\ \delta\mathcal{H}_c'$, which do appear more significant in relation to the rest of the time series. Looking at the extended flare series in Figure 2, there are C- and M-class flares between 70 and 80 hr. Thus, it is possible that the second patch of helicity centered at approximately $(283°,\ 12°)$ contributed to these later events (as potentially did the winding), and the temporal coincidence with the X1.9 flare is down to chance—a warning for any potential predictive method based off of these quantities.

Then, if we consider the combination of parameters $v_z|B_z|$ (Figure 11(a)), a measure of speed of input/removal of flux, we see a spike at 67.2 hr (magenta square), a significant spike in the rate. As with the winding signatures seen at time = 33 hr (Figure 4), the input of flux is centered around the location of the X1.9 flare, and so the spikes seen at both of these times are likely meaningful due to the spatiotemporal proximity to eruptions. Both of these observations indicate that in carefully monitoring related quantities, context may be added to the spikes seen in the winding series.

The main implications of this subsection are that the winding and, to a lesser degree, helicity spikes in the time series are likely a good indicator for the onset of solar eruptions within a given region of the Sun. When analyzed, the signatures of these spikes show strong spatial agreement with the eruptions, as has also been demonstrated for CMEs by O. Aslam et al. (2024). However, the magnitude of the spikes alone, as highlighted by the results for AR 11302, are not likely to be indicative of the magnitude or number of (sympathetic) eruptions.

4.4. Time-series Kurtosis: Gauging the Importance of Spikes

As this manuscript highlighted in Figure 2, AR 11302 exhibits spikes that precede X-class flares, which, when compared to the 2σ envelope, are significant, yet when compared to other spikes in their respective time series, the magnitudes of the spikes appear relatively inconsequential, especially when compared to the X-class magnitude flare that follows shortly after them. One additional quantity we consider in this study is the kurtosis of the ARTop derived time series. Kurtosis is a statistical quantity used to characterize the relative "fatness" of the tails for a probability distribution compared to the mean of the distribution (K. Pearson 1905). Rapid increases in the excess kurtosis have been shown to be an important precursor to system bifurcations (or critical transitions) in a number of fields—for example, in ecological systems (V. Dakos et al. 2019), climate (N. Boers 2018), the economy (C. Sevim et al. 2014), and medicine (L. Chen et al. 2012).

Having explored the spatial distributions of these small spikes in Section 4.3 (e.g., Figure 11), it is difficult to determine from visual inspection whether an input of new topology could contribute to a magnetic reconnection event in the form of a large flare, by comparison to the much more pronounced examples seen for AR 11158 and AR 12673. While this may be something a machine learning model could be trained to determine—something that is beyond the scope of this study—we feel further statistics are likely required that assess the recent behavior of an active region. One we explore here is the excess kurtosis of a given time series, calculated utilizing a kernel width of 3 hr. Examples of this quantity are calculated for the time series of $\delta\mathcal{L}_c'$ and $v_z|B_z|$ for AR 11302 and are shown in Figure 12 during the same observation window as is shown in Figure 2. Values >0 indicate that there is a larger skew in the recent behavior of the given series toward the tails of the series values, by comparison to a normal distribution. That is to say, the series is exhibiting relatively extremal behavior, something that could potentially indicate a system destabilizing and having an increased propensity that some form of eruption may take place.

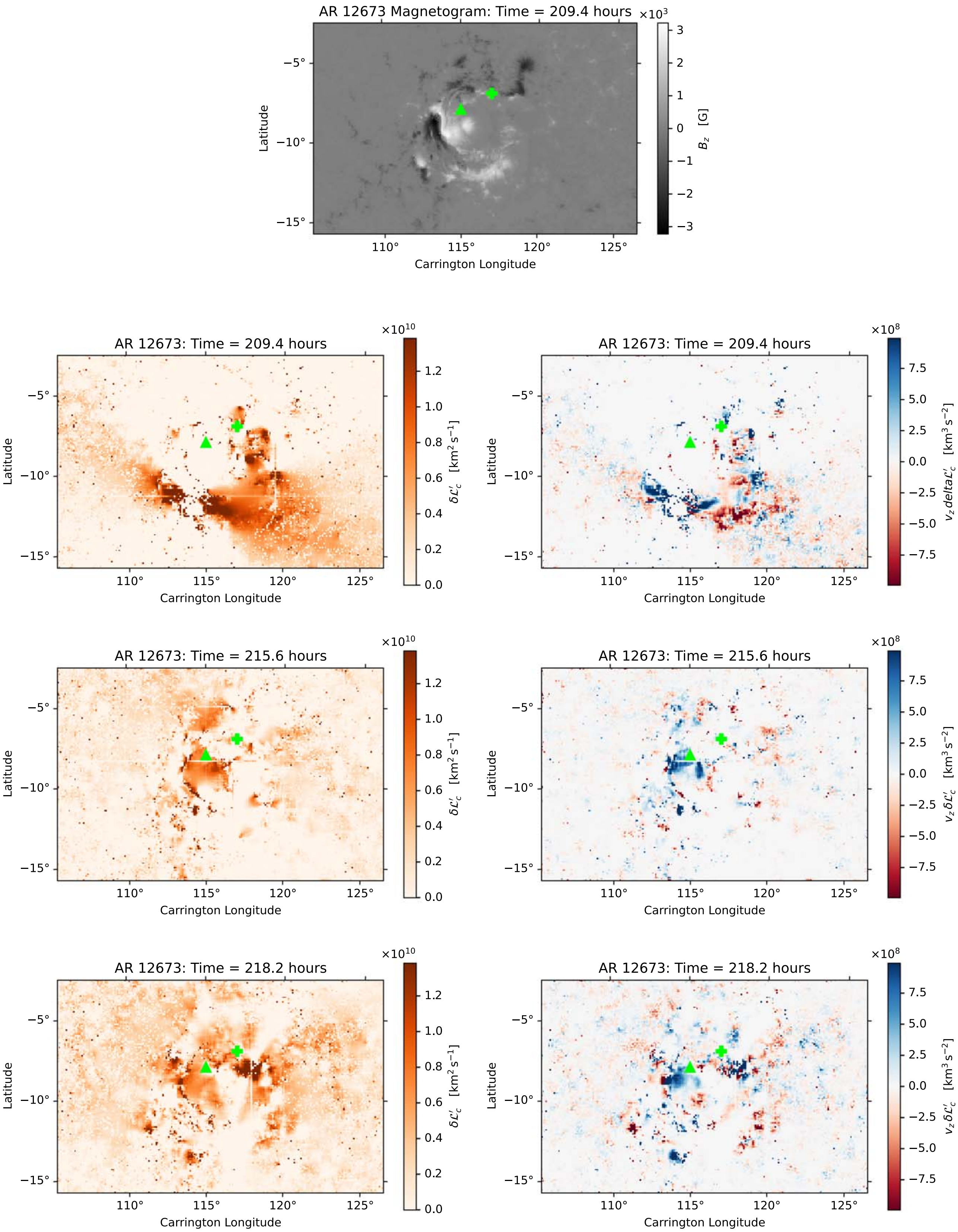

Figure 9. Three snapshots of the $\delta\mathcal{L}'_c$ and $v_z\ \delta\mathcal{L}'_c$ spatial maps from the times corresponding to the three winding spikes that are highlighted by the squares in Figure 8. The position of the X2.2 flare, which erupts just after snapshot 2, is denoted by the lime green plus, while the X9.3 flare position (erupts after snapshot 3) is shown by the lime green triangle. The magnetogram data from this period is shown for spatial reference.

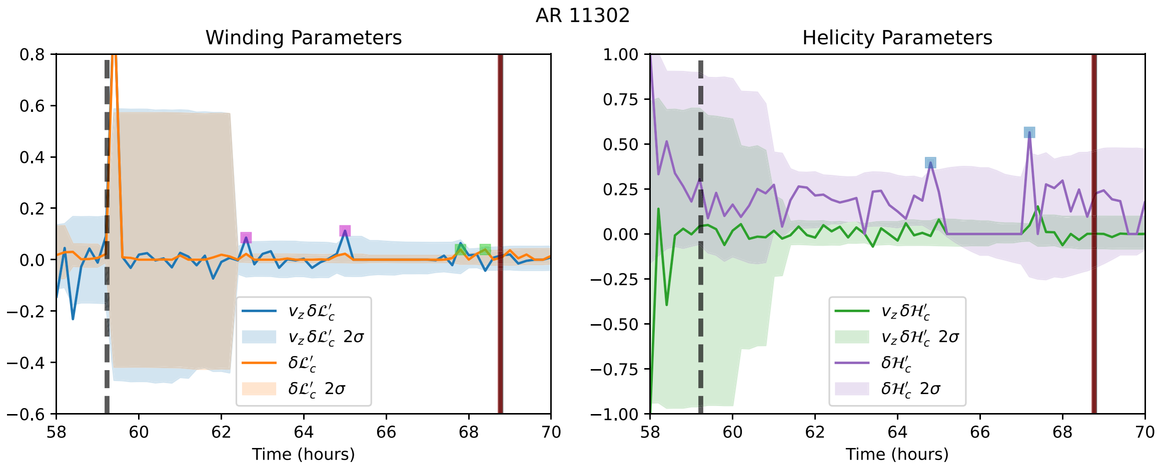

Figure 10. Left: time-series plots for $v_z\ \delta\mathcal{L}_c'$ (blue) and $\delta\mathcal{L}_c'$ (orange) in region AR 12673 for the hours leading to, and including, the X1.9 flare with the corresponding 2σ envelopes denoted by the shaded regions of the same colors. Right: time-series plots for $v_z\ \delta\mathcal{H}_c'$ (green) and $\delta\mathcal{H}_c'$ (magenta) from the same period as Figure 1 with the corresponding 2σ envelopes denoted by the shaded regions of the same colors. The X1.9 flare is indicated by the solid black vertical line, while the M1.9 flare is shown as a dashed black vertical line, and the solitary CME detected by ALMANAC is shown in red.

In these two instances of the excess kurtosis time series shown in Figure 12, its value can be seen to periodically switch between being leptokurtic (excess > 0) and platykurtic (excess < 0), with both being leptokurtic dominant, suggesting that generally, the 3 hr kernel for these quantities has larger tails than a normal distribution. For the X-class flare in AR 11302, we can see that the relative magnitude of the $\delta\mathcal{L}_c'$ excess kurtosis spikes prior to this event (magenta square) has a comparable magnitude to other spikes seen throughout the time series—something that is in stark contrast to the relative size of the $\delta\mathcal{L}_c'$ spikes at the same time (green triangles in Figure 2). It is also worth mentioning that the spike shown here is not the only one that exceeds the 1σ envelope in the few hours immediately before the X-class flare where only minuscule winding signatures are seen (Figure 2; green triangles), as there is a cluster of spikes that exceed this envelope in the period leading to the flare, and so we have only highlighted one of the larger spikes immediately before the X1.9 flare (≈62–69 hr in Figure 12; magenta squares). In the excess kurtosis for $v_z|B_z|$, a similar result to that shown in Figure 11(a) is seen, whereby the spike preceding the flare is one of largest seen across the entire observation window, providing further indication that a potentially large eruption may take place.

In summary, evaluating the excess kurtosis of the time series may provide valuable additional weighting to spikes seen in the original time series when predicting the likelihood of flaring. Individual spikes seen in quantities such as $\delta\mathcal{L}_c'$, provide a glimpse into the instantaneous behavior of the region, while quantities such as the accumulative helicity provide the long-term topology input into a region. The running excess kurtosis complements these statistics by assessing the recent behavior of the region, and quantifying the "tailedness" or extremal nature of its recent behavior. As we have shown in this subsection, a sudden rise in the excess kurtosis could be a key factor in classifying the likely magnitude of a flare.

5. Preliminary Investigations into Forecasting Efficacy

In this section, the focus is on how consistently the quantities outlined in Section 4 may be used to predict the likelihood of flaring. These results should be seen only as a preliminary indication into how frequently spikes in the aforementioned time series correlate with flare activity, rather than the development of a live predictive diagnostic, which is beyond the scope of this study. The aim is to give users an indication to the consistency of each time series with regards to spikes correlating with flares and also how other parameters like the time-integrated δH might be used to classify spikes as meaningful, as discussed in Section 4.

For this, we first analyze the three example regions; AR 11158, AR 11302, and AR 12673 before utilizing a more comprehensive data set (see the Appendix). We define a score, S:

$$S = \frac{1}{2}(X_s + X_f), \tag{13}$$

where X_s and X_f are the percentage of spikes preceding flares within a number of hours (X_s), and the percentage of flares following a spike within a number of hours (X_f), respectively. The first quantity, X_s, quantifies the likelihood a flare being identified with a given spike (in some given metric) within a given period: is this metric good at indicating flares? The second quantity, X_f, attempts to quantify how often a spike can be expected to precede a given flare in a specific period. It is necessary to consider that some metrics, for example, may generate a vast number of spikes and capture almost all flares, but in doing so, too often yield spikes not associated with flares, which would render the metric ineffective. Ideally, the measure will be maximized by metrics that only produce meaningful spikes and do so as consistently as possible.

A weighted score is also defined as S_w, which accounts for the number of spikes and flares within a region. This metric assigns greater importance to regions where flaring is more prominent, but has no dependency on the magnitude of the events. The weighted score is defined by

$$S_w = \frac{1}{2}\left(\frac{\sum_i X_{s_i} N_{s_i}}{\sum_i N_{s_i}} + \frac{\sum_i X_{f_i} N_{f_i}}{\sum_i N_{f_i}}\right), \tag{14}$$

where subscript i indicates the SHARP patch. N_{si} and N_{fi} are the total number of spikes and flares for that region, respectively. If S and S_w provide similar results for a quantity across a number

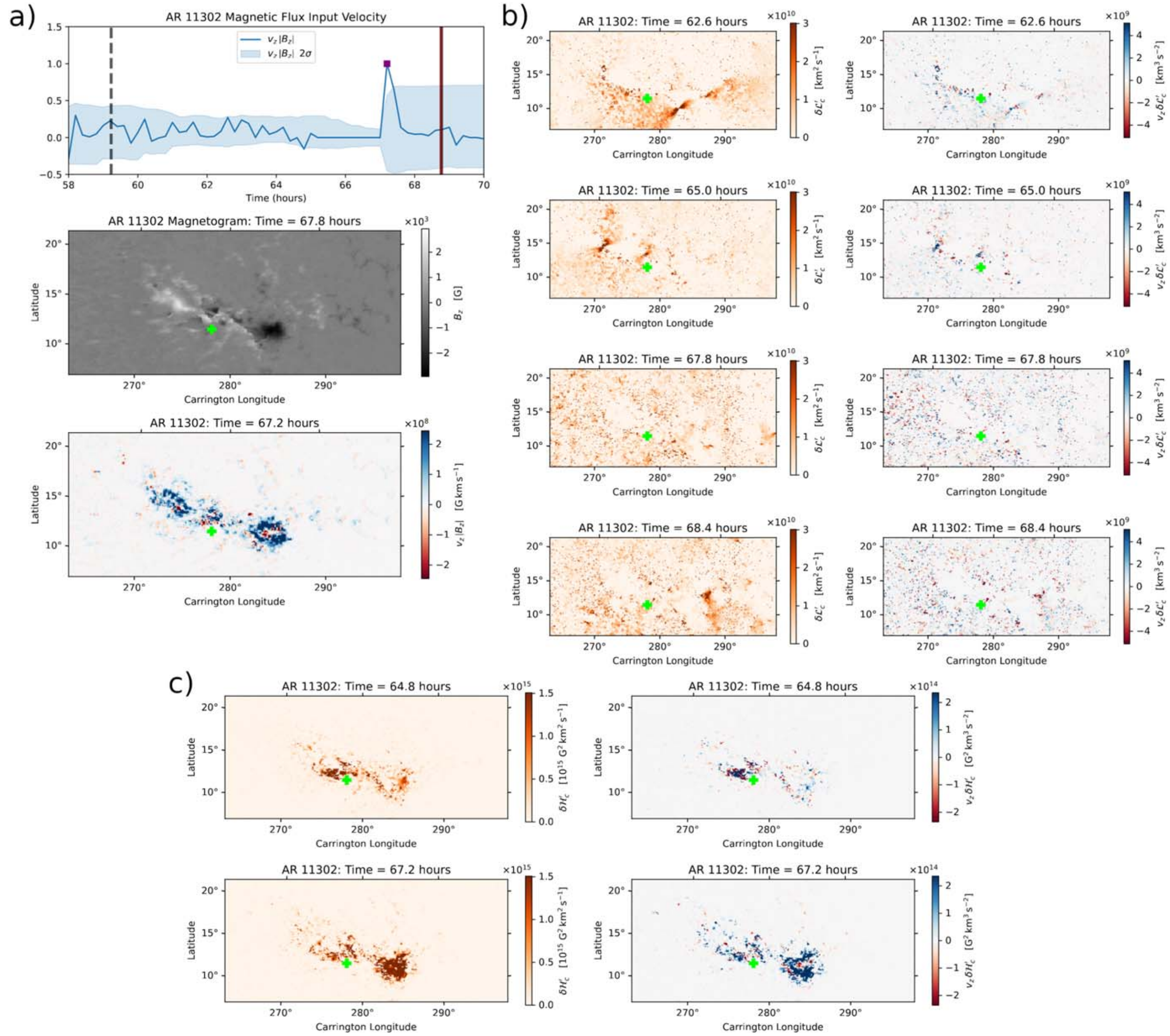

Figure 11. (a) $v_z|B_z|$ time series of AR 11302 in the hours leading up to the X1.9 flare. The magnetogram and $v_z|B_z|$ maps are plotted for the time indicated by the magenta square. (b) Four sets of snapshots of the $\delta\mathcal{L}'_c$ and $v_z\ \delta\mathcal{L}'_c$ spatial maps from the times corresponding to the four winding spikes that are highlighted by the magenta and green squares in Figure 10. (c) Two sets of snapshots corresponding to the times of the blue squares prior to the X1.9 flare in Figure 10. The position of the X1.9 flare, which erupts at $\approx$69 hr, is denoted by the lime green plus in all of the surface maps.

of active regions, it is indicative that the quantity is not biased toward predicting flaring for particular regions over others. However, should S_w drastically exceed S for example, this would indicate a metric is outperforming for active regions with more flare activity, and we should trust it less for less active regions.

5.1. Example Regions

As outlined in Section 4, the quantities determined from ARTop, namely $\delta\mathcal{L}'_c$, $\delta\mathcal{H}'_c$, $v_z\ \delta\mathcal{L}'_c$, $v_z\ \delta\mathcal{H}'_c$, and $v_z|B_z|$ often have spikes that precede flaring, and so the aim here is to quantify the reliability of spikes in these quantities before an eruption. As with the previous Sections, we utilize 3 hr running means and 2σ envelopes for all of the quantities analyzed. As has already been noted in Section 4, some of the earlier spikes in the time series do not lead to flaring, and this typically seems to be when insufficient helicity accumulation has taken place through the photosphere. Consequently, we also quantify the percentage of spikes preceding flares (X_s) and flares preceded by spikes (X_f) with and without a cutoff for the helicity accumulation in Table 2. When employing the helicity cutoff, if a spike exceeding the 2σ envelope is seen in, for example $\delta\mathcal{L}'_c$, but the total helicity accumulation for that active region is below the cutoff, then it is considered to be inconsequential and is omitted from the statistics. Finally, we consider 3, 6, and 12 hr search windows over which we correlate spikes and flares; one would expect that with an increasing search window size that S and S_w would also increase, but in that case, it is less likely one could expect a direct causal relationship between the spike and the flare. We have seen above that it is possible to correlate spikes spatially within periods of up to 9 hr, and so the 12 hr search window here is used to provide some insight into how the metric changes with increased window size.

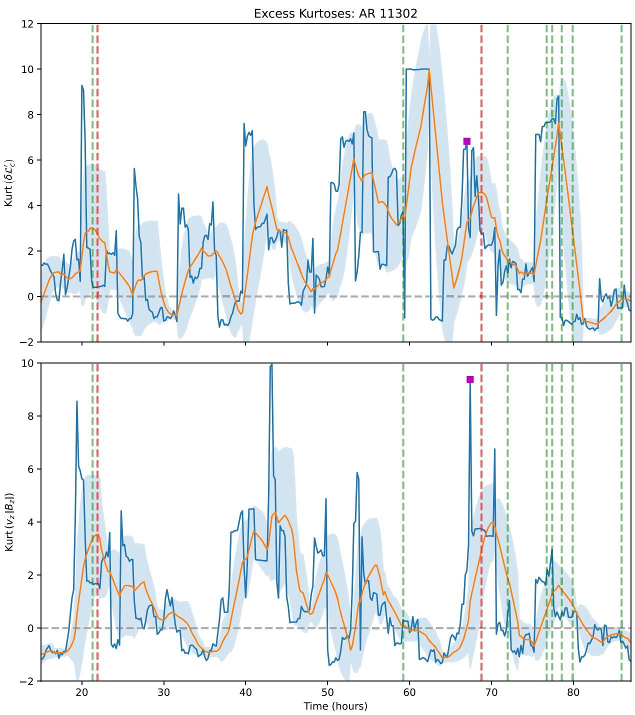

Figure 12. Excess kurtosis plots for $\delta\mathcal{L}_c'$ and $v_z|B_z|$ are shown in blue, with their respective 3 hr running means (orange) and 1σ envelopes shaded blue indicated. The $y = 0$ line (dashed gray) indicates the value for a normal distribution. As with previous Figures, M- and X-class flares are indicated by the dashed vertical green and red lines, respectively. The spikes indicated by the magenta squares correspond to some of the larger peaks seen during the period prior to the flare where there are only minuscule peaks in the winding time-series data (Figure 2; green triangles).

First, we focus on the values of X_s and X_f, which are presented in Table 2 for five quantities and their respective excess kurtoses for the three example regions. We focus on these quantities rather than S and S_w to get an idea of how performance in the two quantities varies. As one would expect, the greater the search duration for a flare (spike) following (preceding) a spike (flare), the larger the percentage of matches seen for X_s (X_f). Without a helicity cutoff, the X_s values show that $\approx$35%−47% of spikes are typically followed by a flare within 3 hr, while $\approx$29%−56% of flares are preceded by spikes (X_f). As that window is broadened to 6 hr and then to 12 hr, X_s and X_f increase with the best scores becoming 69.7% and 85.4%, respectively. However, it is worth noting that only $\delta\mathcal{L}_c'$ and the excess kurtoses have a sufficient number of spikes to be able to "capture" all of the flares from the example regions. When applying a helicity cutoff of 1×10^{19} Mx^2, X_s may improve by as much as 19% ($v_z|B_z|$; 12 hr); however, a more typical improvement is $\approx$7%−8%: spikes are more efficient at correlating with flares. This improvement, however, is to the detriment of X_f, which typically decreases $\approx$1%−2%: fewer flares are caught. Additionally, the total number of spikes (N_s) decreases, which is a positive outcome for $\delta\mathcal{L}_c'$ and the excess kurtoses, as they still exceed the total number of flares (N_f) for the three example regions. This does however further reduce the forecasting efficacy of the other quantities, as their N_s values further decrease below N_f.

We highlight that there are some quantities for which $N_s < N_f$, that is, fewer predictive spikes than there are flares (relatively high X_s and low X_f). These will tend to perform worse with a cutoff, while those for which $N_s > N_f$ are candidates for improvement. Intriguingly, while it is only $\delta\mathcal{L}_c'$ of the raw quantities that has $N_s > N_f$, marking it as a key quantity in this data set, the excess kurtosis of all of the explored quantities has this property.

5.2. Flare Prediction on Large Data Set

We now turn our attention to the full data set given in the Appendix. For this, a number of combinations of the parameters that define spikes are tested, namely, the running mean period, the standard deviation envelope size (outside of which the signal must rise to yield a spike), and the helicity cutoff, which further refines the definition of a meaningful spike or signal (Table 3). The results for the best 10 performing combinations (largest value of the mean $\frac{S+S_w}{2}$) are shown in Tables 4–6, calculated on the 65 SHARP regions that undergo flaring. As above, search windows within 3, 6, and 12 hr of a spike are considered for linking spikes to flares. N_s is also provided for each quantity and parameter combination to show the number of false-positive detections in the 79 SHARP regions that have no associated flare activity (we focus on this data shortly).

Immediately, it is apparent that regardless of the period after a spike that is being analyzed (i.e., is there a flare?), it is $\delta\mathcal{L}_c'$ or quantities derived from this that consistently have the best scores for both measures S and S_w. As with Table 2, S, S_w, and $\frac{S+S_w}{2}$ all improve in their accuracy as indicators for flaring when the search window is increased to 12 hr. Although, the increase here is $\approx$20%, whereas for the three example regions, with numerous, high-energy eruptions, a value of $\approx$30% was obtained. We also note that scores are slightly down on the values found for our three example regions (e.g., S for 3 hr goes from 47% down to 38%). We also reflect on the fact the S_w scores are consistently higher than their unweighted counterparts. Many of the regions included have only smaller C-class flares and/or only one or two flares. Subsequently, it is clear that the metrics investigated here are providing more meaningful value in more flare-rich regions.

On shorter timescales, particularly within 3 hr of a spike (Table 4), $\delta\mathcal{L}_c'$ occupies four of the top 10 scores, and as with the example shown in Figure 12, the excess kurtosis calculations also provide comparatively good scores along with $v_z\ \delta\mathcal{L}_c'$. As the search window size increases, the parameters in the top 10 lists become more varied, with the velocity combinations and their excess kurtoses becoming more prevalent.

5.2.1. False Positives

Perhaps unsurprisingly due to the nature of S and S_w, the majority of top 10 scores do not include a helicity cutoff and prefer smaller running mean envelopes, σ. Increasing these two parameters drastically reduces the number of false-positive detections seen in the nonflaring regions (N_s in Tables 4–6). For example, $\delta\mathcal{L}_c'$ calculated (Table 4) with a running mean of 3 hr, $\sigma = 1.5$, and a helicity cutoff of 1×10^{18} Mx^2 yields scores of $S = 0.311$, $S_w = 0.406$, and $\frac{S+S_w}{2} = 0.359$, while only having $N_s = 2672$ across the 79 nonflaring region compared to $N_s = 4752$ without the cutoff. However, as outlined earlier, when S_w significantly exceeds S for a metric, this suggests that the metric is outperforming for larger, more active SHARP

Table 2
Percentage of Spikes Preceding Flares, X_s, and Flares with Spikes Preceding them, X_f, across the Three Example Regions

Quantity	X_s 3 hr	X_s 6 hr	X_s 12 hr	N_s	X_f 3 hr	X_f 6 hr	X_f 12 hr	N_f
No Helicity Cutoff Applied								
$\delta\mathcal{L}_c'$	0.470	0.566	0.697	236	0.556	0.756	0.848	190
$\delta\mathcal{H}_c'$	0.380	0.502	0.653	166	0.371	0.549	0.737	190
$v_z\ \delta\mathcal{L}_c'$	0.383	0.494	0.652	163	0.383	0.608	0.790	190
$v_z\ \delta\mathcal{H}_c'$	0.356	0.518	0.648	156	0.349	0.574	0.749	190
$v_z\|B_z\|$	0.402	0.512	0.608	113	0.291	0.537	0.735	190
Kurt($\delta\mathcal{L}_c{}'$)	0.428	0.551	0.644	291	0.474	0.702	0.803	190
Kurt($\delta\mathcal{H}_c{}'$)	0.359	0.512	0.646	261	0.423	0.688	0.854	190
Kurt($v_z\ \delta\mathcal{L}_c{}'$)	0.470	0.600	0.669	265	0.401	0.721	0.842	190
Kurt($v_z\ \delta\mathcal{H}_c{}'$)	0.399	0.539	0.616	289	0.477	0.681	0.850	190
Kurt($v_z\ \|B_z\|$)	0.452	0.546	0.668	269	0.433	0.677	0.835	190
Helicity Cutoff of 1×10^{19} Mx^2 Applied								
$\delta\mathcal{L}_c'$	0.554	0.654	0.785	207	0.545	0.728	0.814	190
$\delta\mathcal{H}_c'$	0.469	0.631	0.769	134	0.355	0.521	0.698	190
$v_z\ \delta\mathcal{L}_c'$	0.462	0.597	0.743	138	0.366	0.575	0.751	190
$v_z\ \delta\mathcal{H}_c'$	0.465	0.694	0.806	118	0.327	0.540	0.716	190
$v_z\|B_z\|$	0.564	0.688	0.791	92	0.280	0.514	0.707	190
Kurt($\delta\mathcal{L}_c{}'$)	0.519	0.658	0.738	257	0.474	0.691	0.787	190
Kurt($\delta\mathcal{H}_c{}'$)	0.400	0.569	0.714	231	0.406	0.655	0.821	190
Kurt($v_z\ \delta\mathcal{L}_c{}'$)	0.527	0.671	0.736	239	0.379	0.688	0.803	190
Kurt($v_z\ \delta\mathcal{H}_c{}'$)	0.487	0.633	0.723	250	0.471	0.658	0.822	190
Kurt($v_z\ \|B_z\|$)	0.512	0.611	0.728	243	0.422	0.649	0.802	190

Table 3
List of Parameter Scans Performed

Run. Mean. (hr)	σ	Helicity Cutoff (Mx^2)
3	1.5	0
6	2.0	1×10^{18}
9	2.5	1×10^{19}
12	3.0	1×10^{20}

regions, and should be considered less effective for less active SHARP regions.

We now focus on nonflaring regions whose metric performance is represented by the quantity N_s, in effect the number of errors made. It is found that higher helicity cutoffs reduced the number N_s at the cost of significantly lower S and S_w on the flaring regions. The quantities shown here are grossly unreliable for nonflaring regions with thousands of false positives across the data set. While this manuscript demonstrates that there is clear merit to the topological quantities in regards to spikes preceding flare activity. It may be that a balance could be realized by combining various metrics with more stringent thresholds/cutoffs and employing some form of neural network to predict flaring based on all of the metrics produced—a significant endeavor beyond the scope of this study.

The final point we make in this study is that a productive approach to the issue of the metrics being significantly misleading for nonflaring regions, might be to try to use the data to first classify regions as flaring or not. If one could identify the regions that do and do not flare, then the metrics could be applied to make individual flare predictions, and the above results indicate they have some potential in that regard, especially in the more active regions that have X-class flares. In Figure 13, we see a scatter plot for all 144 SHARP regions' maximum values for accumulated (time-integrated) $\delta\mathcal{L}_c'$ and $\delta\mathcal{H}_c'$. Each region is color-coded depending on the classification of the maximum flare magnitude associated with that region; X-class (red), M-class (orange), C-class (green), and nonflaring (blue). As one would expect, there is a strong correlation between the maximum accumulated $\delta\mathcal{L}_c'$ and $\delta\mathcal{H}_c'$ values given that magnetic winding is derived from magnetic helicity. However, for the flaring regions, there does appear to be a positive trend in the amount of topology accumulated and the maximum magnitude of flare seen. More explicitly, all of the active regions with associated X-class flares are situated to the upper-right quadrant of the scatter plot, as are (proportionally) more of the active regions with M-class and C-class flares. If maximum accumulated values exceeding 6×10^{15} cm^4 and 1×10^{20} Mx^2 are seen for $\delta\mathcal{L}_c'$ and $\delta\mathcal{H}_c'$, respectively, then there is a high probability of the region flaring (according to this data set) with only three nonflaring regions exceeding these values from our data set, while all regions with X-class flares are captured. Additionally, visual inspection of the nonflaring region(s) in question, such as the three randomly selected regions shown in the panels on the right of Figure 13, reveals that many nonflaring regions are either small or in their

Table 4
Ten Best-performing Statistics in Both S and S_w across All 65 SHARP Regions Analyzed with Flare Activity within 3 hr of a Spike

Quantity	Run. Mean (hr)	σ	Helicity Cutoff (Mx^2)	S	S_w	$\frac{1}{2}(S+S_W)$	N_s (Nonflaring)
$\delta\mathcal{L}_c'$	3	1.5	0	0.376	0.408	0.392	4752
$\delta\mathcal{L}_c'$	3	1.5	1×10^{18}	0.311	0.406	0.359	2672
$\delta\mathcal{L}_c'$	6	1.5	0	0.33	0.354	0.342	4499
$v_z\ \delta\mathcal{L}_c'$	3	1.5	0	0.325	0.344	0.335	3712
Kurt($v_z\ \delta\mathcal{H}_c{}'$)	3	1.5	0	0.308	0.359	0.333	7942
Kurt($v_z\ \|B_z\|$)	3	1.5	0	0.301	0.362	0.331	7741
$v_z\ \delta\mathcal{H}_c'$	3	1.5	0	0.321	0.337	0.329	4192
$\delta\mathcal{H}_c'$	3	1.5	0	0.303	0.348	0.326	4797
$\delta\mathcal{L}_c'$	3	2	0	0.314	0.337	0.325	2655
Kurt($v_z\ \delta\mathcal{L}_c{}'$)	3	1.5	0	0.31	0.34	0.325	7796

Table 5
Ten Best-performing Statistics in Both S and S_w across All 65 SHARP Regions Analyzed with Flare Activity within 6 hr of a Spike

Quantity	Run. Mean (hr)	σ	Helicity Cutoff (Mx^2)	S	S_w	$\frac{1}{2}(S+S_W)$	N_s (Nonflaring)
$\delta\mathcal{L}_c'$	3	1.5	0	0.467	0.527	0.497	4752
$v_z\ \delta\mathcal{L}_c'$	3	1.5	0	0.456	0.497	0.476	3712
Kurt($v_z\ \delta\mathcal{H}_c{}'$)	3	1.5	0	0.447	0.5	0.473	7942
$\delta\mathcal{L}_c'$	6	1.5	0	0.446	0.496	0.471	4499
$v_z\ \delta\mathcal{H}_c'$	3	1.5	0	0.447	0.482	0.465	4192
Kurt($v_z\ \|B_z\|$)	3	1.5	0	0.427	0.494	0.461	7741
Kurt($v_z\ \delta\mathcal{L}_c{}'$)	3	1.5	0	0.429	0.484	0.457	7796
$\delta\mathcal{L}_c'$	3	2	0	0.428	0.485	0.456	2655
$\delta\mathcal{L}_c'$	3	1.5	1×10^{18}	0.385	0.528	0.456	2672
Kurt($\delta\mathcal{L}_c{}'$)	3	1.5	0	0.417	0.487	0.452	7475

Table 6
Ten Best-performing Statistics in Both S and S_w across All 65 SHARP Regions Analyzed with Flare Activity within 12 hr of a Spike

Quantity	Run. Mean (hr)	σ	Helicity Cutoff (Mx^2)	S	S_w	$\frac{1}{2}(S+S_W)$	N_s (Nonflaring)
$\delta\mathcal{L}_c'$	3	1.5	0	0.536	0.598	0.567	4752
$v_z\ \delta\mathcal{L}_c'$	3	1.5	0	0.535	0.585	0.56	3712
$\delta\mathcal{L}_c'$	6	1.5	0	0.529	0.587	0.558	4499
Kurt($v_z\ \|B_z\|$)	3	1.5	0	0.53	0.585	0.557	7741
$v_z\ \delta\mathcal{H}_c'$	3	1.5	0	0.533	0.579	0.556	4192
$\delta\mathcal{L}_c'$	3	2	0	0.519	0.593	0.556	2655
$v_z\|B_z\|$	3	1.5	0	0.529	0.582	0.556	4314
Kurt($v_z\ \delta\mathcal{H}_c{}'$)	3	1.5	0	0.529	0.581	0.555	7942
Kurt($v_z\ \|B_z\|$)	3	2	0	0.524	0.58	0.552	4001
Kurt($v_z\ \delta\mathcal{H}_c{}'$)	3	2	0	0.526	0.577	0.551	4117

decaying phases. As such, they exhibit diffuse magnetograms with no prominent concentrations of magnetic flux. This "diffusiveness," particularly for large SHARP patches, may explain how large accumulations of winding and helicity are not always associated with flares. That is, modest concentrations of topology are inputted over large areas. Subsequently, the localized concentrations required to create complex magnetic field configurations within the solar atmosphere that can become perturbed and trigger a reconnection event are not met, and no flaring occurs. There are numerous existing methods for classifying regions (P. S. McIntosh 1990; L. Kashapova et al. 2021), and in some cases, those that are automated (L. S. de Oliveira & A. L. S. Gradvohl 2020), which could be combined with these maximum $\delta\mathcal{L}_c'$ and $\delta\mathcal{H}_c'$ values to separate out flaring and nonflaring regions. We hope that by making this data set available, other researchers could effectively address this question.

In summary, the results presented in Section 5 provide a valuable first step in transforming the ARTop topology calculations into predictive metrics for solar eruptions. Within flaring active regions, ≈40%–60% of spikes and flares can be associated to one another, with $\delta\mathcal{L}_c'$ providing the most promising results/scores.

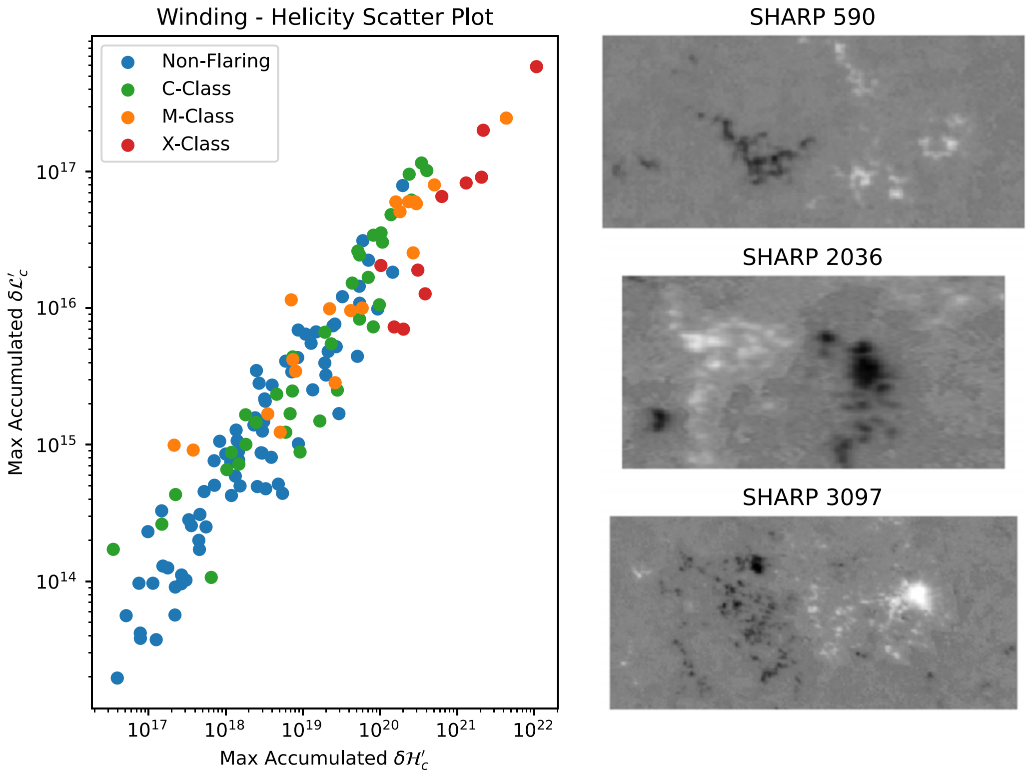

Figure 13. Left: log–log scatter plot for maximum values of accumulated $\delta\mathcal{L}'_c$ and $\delta\mathcal{H}'_c$ for the 144 SHARP regions analyzed. Color is coded based on the class of the maximum flare magnitude given by the legend. Right: three typical magnetograms from nonflaring SHARP regions that have been chosen at random for display.

6. Conclusions

This manuscript presents analysis on the quantities $\delta\mathcal{L}'_c$, $\delta\mathcal{H}'_c$, $v_z\ \delta\mathcal{L}'_c$, $v_z\ \delta\mathcal{H}'_c$, $v_z|B_z|$ (and their accumulated and kurtosis values) as calculated by the ARTop package, and assess their potential efficacy for flare prediction. They are applied to time series of flaring across 144 (65 flaring; 79 nonflaring) active regions contained within SHARP data sets. A region is considered to be flaring in this study if it has a reported X-ray flare class equal to, or exceeding C1.0 within HEK. The key findings from this study are listed as follows:

1. The δ measures of the winding and helicity rates provided by the ARTop package, which measure the net imbalance of current-carrying over potential field derived topological fluxes, greatly reduces the dependence on the VS parameter, which is used when creating velocity maps from magnetogram data using the DAVE4VM method. As this work highlights, more frequently employed topological quantities like the helicity and winding fluxes are sensitive to this choice, and depending on the values selected, this may mean photospheric signatures are not detected until after an eruption has occurred.
2. Constructing time series ($\delta\mathcal{L}'_c$ and $\delta\mathcal{H}'_c$) composed of only the current-carrying-dominant parts of the δL and δH fluxes produced time series whose extremal values, spikes (those outside of two standard deviations from the running mean over a suitable window) show significant temporal correlation with the timing of flares. When these signals are only classified as meaningful if a significant amount of net current-carrying helicity δH has been accumulated in the region, this correlation improves significantly. It is further shown that a number of the spikes showed a spatiotemporal correlation with the sites of X-class flares, which are cotemporal with CME events. This provides evidence that these spikes can provide physically meaningful signals.
3. Across the parameter scans for the metrics investigated in this work, it seems that $\delta\mathcal{L}'_c$ is the topological quantity with the greatest potential for forecasting flaring events on its own (based on spiking activity of the quantities examined during this study). Additionally, we found there is some benefit to adopting an helicity cutoff when determining if a spike should be counted as a meaningful event. We hypothesize that the cutoff acts as a means of quantifying whether there is a sufficient complex magnetic field residing above the photosphere for new topology input to destabilize existing structures to cause reconnection events. Such an adoption yielded approximately half the number of false-positive spikes in nonflaring regions for $\delta\mathcal{L}'_c$ with other, more stringent cutoffs, reducing this much further, albeit at the cost of further reduced efficacy for predicting flares. We present evidence that some algorithm that could deduce whether a region is likely to flare would allow the quantities derived in this study to form the basis for a predictive methodology for individual flare events.
4. The majority of the parameter combinations presented in the data set (except $\delta\mathcal{L}'_c$) do not generate more spikes than there are flares for the subset of three regions (ARs 11158, 11302, and 12673), which are analyzed in detail. However, a similar spike-based analysis of the excess kurtosis for these metrics improved their ability to identify flares, becoming more comparable to $\delta\mathcal{L}'_c$, while also increasing the number of spikes such that there are

more spikes than the number of flares. The excess kurtoses provide a compliment to the short-term (i.e., $\delta\mathcal{L}_c'$, $\delta\mathcal{H}_c'$, $v_z|B_z|$, etc.) and long-term (accumulated winding and helicity) metrics determined by ARTop, by providing a medium-term memory of the time series. It is also shown in Section 4.4 that the kurtosis of the time series might be used in conjunction with the $\delta\mathcal{L}_c'$ time series to anticipate the magnitude of a flare (predictive signal).

The data set used for this manuscript is publicly available as a pickle file along with some sample Jupyter Notebooks on how to process the data.[4] This is a living database and will continually grow as more regions are processed with the ARTop code. This database will form the basis of a predictive model to further test the efficacy of topology calculations when it comes to forecasting the likelihood and potential magnitude of flaring events. As mentioned earlier, there are currently a large number of false-positive spikes, especially in nonflaring regions, though it may be possible to segregate flaring and nonflaring regions based on the ratio of maximum accumulated winding and helicity and/or the visual appearance of magnetogram data, i.e., how diffuse/complex the region is. The issues identified here will be addressed in a future study.

Acknowledgments

The authors acknowledge support from the US Air Force grant FA8655-23-1-7247. D.M. acknowledges support from a Leverhulme Trust grant (RPG-2023-182), a Science and Technologies Facilities Council (STFC) grant (ST/Y001672/1) and a Personal Fellowship from the Royal Society of Edinburgh (ID:4282). C.P. acknowledges support from The UK Science and Technology Funding Council under grant No. ST/W00108X/1. This research utilizes version 5.1.2 of the SunPy open-source software package (S. J. Mumford et al. 2024).

Appendix

Here, the full list of 144 SHARP regions used for this study are given in Table 7. A breakdown on the largest flare size, as well as the total number of X-, M-, and C-class flares is given for each region. In total, 65 regions exhibit flaring, with a further 79 regions being flare free.

[4] Github: https://github.com/DrTomWilliams/Machine-Learning-Flare-Dataset.

Table 7
SHARP Regions Investigated with Flare Information Provided by HEK

NOAA Active Region	SHARP Number	Largest Flare	No. X-class Flares	No. M-class Flares	No. C-class Flares
11069	8	M1.2	…	1	7
11070	14	…	…	…	…
11071	17	…	…	…	…
11072	26	…	…	…	…
11076	43	…	…	…	…
11073/77	45	…	…	…	…
11079	49	M1.0	…	1	…
11080	51	C1.2	…	…	1
11081	54	M2.0	…	1	5
11086	83	…	…	…	…
11087	86	C3.4	…	…	5
11096	116	…	…	…	…
11098	131	…	…	…	…
11105	156	C3.3	…	…	2
11114	219	…	…	…	…
11116	221	…	…	…	…
11121/23	245	M5.4	…	3	18
11130	274	…	…	…	…
11132	285	…	…	…	…
11136	316	…	…	…	…
11138	318	C1.3	…	…	1
11141	325	C1.9	…	…	1
11143	335	…	…	…	…
11148	347	…	…	…	…
11151	354	…	…	…	…
11155	366	…	…	…	…
11156	367	…	…	…	…
11158	377	X2.2	1	5	54
11160/61/62	384	M1.3	…	4	20
11165	394	M5.3	…	6	24
11172/75	421	C1.6	…	…	2
11173	429	…	…	…	…
11179	436	…	…	…	…
11176/78	437	M1.4	…	3	13
11177	438	…	…	…	…
11198	527	…	…	…	…
11199	540	C6.5	…	…	5
11206	572	…	…	…	…
11209	589	…	…	…	…
11211	590	…	…	…	…
11212	595	…	…	…	…
11214/17	602	…	…	…	…
11221	619	…	…	…	…
11219/24	622	C5.9	…	…	2
11223	625	C1.4	…	…	2
11242	686	…	…	…	…
11245/53	700	…	…	…	…
11248/53/57	705	…	…	…	…
11258	713	…	…	…	…
11273	799	…	…	…	…
11281	824	…	…	…	…
11283	833	X2.1	2	5	13
11291	851	…	…	…	…
11300	875	…	…	…	…
…	877	C9.6	…	…	15
11302	892	X1.9	2	15	31
11311	926	…	…	…	…
11314/19	940	M1.3	…	2	32
11318	956	…	…	…	…
11327	982	…	…	…	…
11326	990	…	…	…	…
11339/48	1028	X1.9	1	11	47
11341/42	1041	M1.1	…	1	3
11357	1080	C1.8	…	…	3
11373	1170	…	…	…	…
11380/87	1209	M4.0	…	3	11
11385	1232	…	…	…	…
11398	1303	…	…	…	…
11397	1312	…	…	…	…
11416	1389	C1.5	…	…	1
11420	1399	…	…	…	…
11429/30	1449	X5.4	3	14	36
11434	1464	…	…	…	…
11437	1480	…	…	…	…
11446	1497	…	…	…	…
11450	1528	C3.1	…	…	5
11463	1558	C8.9	…	…	5
11456	1564	…	…	…	…
11460/64	1578	C3.7	…	…	5
11464	1594	…	…	…	…
11466/68	1603	M1.0	…	1	4
11469/73	1611	C2.6	…	…	12
11476	1638	M5.7	…	11	84
11477/78	1644	…	…	…	…
11488	1688	…	…	…	…
11523	1863	…	…	…	…
11527/28	1877	C5.0	…	…	7
11531	1886	C1.7	…	…	2
11546	1942	…	…	…	…
11547	1943	…	…	…	…
11548	1946	M5.5	…	5	11
11549	1948	…	…	…	…
11554	1962	C7.6	…	…	5
11562	1990	C8.4	…	…	2
11560	1993	M1.6	…	1	17
11561	1997	…	…	…	…
11565	2007	C2.3	…	…	2
11568	2017	C1.7	…	…	1
11572	2036	…	…	…	…
11591	2121	…	…	…	…
11598	2137	X1.8	1	3	23
11601	2158	…	…	…	…
11613/17	2191	M6.0	…	5	15
11628/29	2262	C5.7	…	…	3
11630	2270	C5.5	…	…	2
11631/32	2291	C1.4	…	…	6
11640	2337	C4.0	…	…	6
11651	2348	…	…	…	…
11664	2425	…	…	…	…
11668	2436	…	…	…	…
11682	2501	…	…	…	…
11680	2504	…	…	…	…
11696	2560	C2.2	…	…	2
11719	2635	M6.5	…	2	13
11737	2711	…	…	…	…
11748	2748	X3.2	3	3	18
11752	2754	C1.3	…	…	3
11768	2832	…	…	…	…
11784	2922	C1.1	…	…	1
11796	2976	…	…	…	…
11809	3028	C4.9	…	…	9
11821	3079	…	…	…	…

Table 7
(Continued)

NOAA Active Region	SHARP Number	Largest Flare	No. X-class Flares	No. M-class Flares	No. C-class Flares
11824	3097	…	…	…	…
11835	3122	…	…	…	…
11881	3309	…	…	…	…
11892	3353	…	…	…	…
11905	3420	C3.3	…	…	6
11916	3448	C3.3	…	…	6
11930	3515	C1.8	…	…	3
11942	3560	…	…	…	…
11967/72/75	3686	M6.6	…	23	66
11978	3741	…	…	…	…
11996	3813	M9.3	…	4	10
12009	3853	…	…	…	…
12024	3907	C2.4	…	…	1
12036/37/43	3999	M7.3	…	1	27
12050	4075	C1.1	…	…	1
12066	4131	…	…	…	…
12089	4231	…	…	…	…
12111	4328	…	…	…	…
12192	4698	X3.1	6	32	72
12268/70/79	5107	M2.1	…	6	31
12297	5298	X2.1	1	22	92
12673	7115	X9.3	4	26	52

ORCID iDs

Thomas Williams https://orcid.org/0000-0002-2006-6096
Christopher B. Prior https://orcid.org/0000-0003-4015-5106
David MacTaggart https://orcid.org/0000-0003-2297-9312

References

Alielden, K., MacTaggart, D., Ming, Q., Prior, C., & Raphaldini, B. 2023, RASTI, 2, 398
Aslam, O., MacTaggart, D., Williams, T., Fletcher, L., & Romano, P. 2024, MNRAS, 534, 444
Berger, M. A. 1984, GApFD, 30, 79
Bi, Y., Liu, Y. D., Liu, Y., et al. 2018, ApJ, 865, 139
Boers, N. 2018, NatCo, 9, 2556
Chen, L., Liu, R., Liu, Z.-P., Li, M., & Aihara, K. 2012, NatSR, 2, 342
Dakos, V., Matthews, B., Hendry, A. P., et al. 2019, NatEE, 3, 355
de Oliveira, L. S., & Gradvohl, A. L. S. 2020, Revista Brasileira de Computação Aplicada, 12, 67
Garland, S. H., Yurchyshyn, V. B., Loper, R. D., Akers, B. F., & Emmons, D. J. 2024, FrASS, 11, 1369749
Georgoulis, M. K., Bloomfield, D. S., Piana, M., et al. 2021, JSWSC, 11, 39
Hoeksema, J. T., Liu, Y., Hayashi, K., et al. 2014, SoPh, 289, 3483
Hollanda, A., Antunes Da Silva, A. E., & Cinto, T. 2021, DIB, 37, 107203
Hurlburt, N. E. 2022, AGUFM, 2022, SH32F–1818
Jarolim, R., Thalmann, J., Veronig, A., & Podladchikova, T. 2023, NatAs, 7, 1171
Kashapova, L., Zhukova, A., Miteva, R., et al. 2021, Ge&Ae, 61, 1022
Knizhnik, K. J., Antiochos, S. K., & DeVore, C. R. 2015, ApJ, 809, 137
Korsós, M., Erdélyi, R., Huang, X., & Morgan, H. 2022, ApJ, 933, 66
Korsós, M., Romano, P., Morgan, H., et al. 2020, ApJL, 897, L23
Kusano, K., Iju, T., Bamba, Y., & Inoue, S. 2020, Sci, 369, 587
LaBonte, B., Georgoulis, M., & Rust, D. 2007, ApJ, 671, 955
Leka, K., Park, S.-H., Kusano, K., et al. 2019a, ApJS, 243, 36
Leka, K., Park, S.-H., Kusano, K., et al. 2019b, ApJ, 881, 101
Lemen, J. R., Title, A. M., Akin, D. J., et al. 2012, SoPh, 275, 17
Liu, L., Cheng, X., Wang, Y., & Zhou, Z. 2019, ApJ, 884, 45
Liu, Y., & Schuck, P. 2012, ApJ, 761, 105
Liu, Y., Welsch, B. T., Valori, G., et al. 2023, ApJ, 942, 27
Lumme, E., Kazachenko, M., Fisher, G., et al. 2019, SoPh, 294, 84
MacTaggart, D., Prior, C., Raphaldini, B., Romano, P., & Guglielmino, S. L. 2021, NatCo, 12, 6621
McIntosh, P. S. 1990, SoPh, 125, 251
Moraitis, K., Patsourakos, S., Nindos, A., Thalmann, J., & Pariat, É. 2024, A&A, 683, A87
Moraitis, K., Sun, X., Pariat, É., & Linan, L. 2019, A&A, 628, A50
Mumford, S. J., Freij, N., Stansby, D., et al. 2024, SunPy, v5.1.1, Zenodo, doi:10.5281/zenodo.591887
Nindos, A., Zhang, J., & Zhang, H. 2003, ApJ, 594, 1033
Pariat, E., Démoulin, P., & Berger, M. A. 2005, A&A, 439, 1191
Pariat, E., Leake, J., Valori, G., et al. 2017, A&A, 601, A125
Pariat, E., Nindos, A., Démoulin, P., & Berger, M. 2006, A&A, 452, 623
Park, S.-H., Chae, J., & Wang, H. 2010, ApJ, 718, 43
Park, S.-H., Lee, J., Choe, G.-S., et al. 2008, ApJ, 686, 1397
Park, S.-H., Leka, K., & Kusano, K. 2021, ApJ, 911, 79
Pearson, K. 1905, Biometrika, 4, 169
Pevtsov, A. A., Maleev, V. M., & Longcope, D. W. 2003, ApJ, 593, 1217
Price, D. J., Pomoell, J., Lumme, E., & Kilpua, E. K. J. 2019, A&A, 628, A114
Priest, E. R., Longcope, D., & Janvier, M. 2016, SoPh, 291, 2017
Prior, C., & MacTaggart, D. 2020, RSPSA, 476, 20200483
Raphaldini, B., Dikpati, M., Norton, A. A., et al. 2023, ApJ, 958, 175
Raphaldini, B., Prior, C. B., & MacTaggart, D. 2022, ApJ, 927, 156
Schou, J., Scherrer, P. H., Bush, R. I., et al. 2012, SoPh, 275, 229
Schuck, P. W. 2008, ApJ, 683, 1134
Sevim, C., Oztekin, A., Bali, O., Gumus, S., & Guresen, E. 2014, Eur. J. Operational Research, 237, 1095
Thalmann, J. K., Moraitis, K., Linan, L., et al. 2019, ApJ, 887, 64
Tziotziou, K., Georgoulis, M. K., & Liu, Y. 2013, ApJ, 772, 115
Vemareddy, P. 2019, ApJ, 872, 182
Vemareddy, P. 2021, MNRAS, 507, 6037
Wang, R., Liu, Y. D., Hoeksema, J. T., Zimovets, I., & Liu, Y. 2018, ApJ, 869, 90
Williams, T., & Morgan, H. 2022, SpWea, 20, e2022SW003253
Zuccarello, F. P., Pariat, E., Valori, G., & Linan, L. 2018, ApJ, 863, 41